The ^{26}Al-^{26}Mg systematics of FeO-rich chondrules from Acfer 094: two chondrule generations distinct in age and oxygen isotope ratios

Andreas T. Hertwig[1]*, Kimura Makoto[2], Takayuki Ushikubo[3], Céline Defouilloy[1], and Noriko T. Kita[1]

[1] WiscSIMS, Department of Geoscience, University of Wisconsin-Madison, Madison, WI 53706, USA

[2] National Institute of Polar Research, Meteorite Research Center, Midoricho 10-3, Tachikawa, Tokyo 190-8518, Japan

[3] Kochi Institute for Core Sample Research, JAMSTEC, 200 Monobe-otsu, Nankoku, Kochi 783-8502 Japan

* Corresponding author, present address: Department of Earth, Planetary, and Space Sciences, University of California-Los Angeles, Los Angeles, CA 90095, USA

Abstract

The ^{26}Al-^{26}Mg ages of FeO-rich (type II) chondrules from Acfer 094, one of the least thermally metamorphosed carbonaceous chondrites, were determined by SIMS analysis of plagioclase and olivine/pyroxene using a radio frequency (RF) plasma oxygen ion source. In combination with preexisting ^{26}Al-^{26}Mg ages of FeO-poor (type I) chondrules, the maximum range of formation ages recorded in chondrules from a single meteorite is determined to help provide constraints on models of material transport in the proto-planetary disk. We also report new SIMS oxygen three-isotope analyses of type II chondrules in Acfer 094. All but one of the plagioclase analyses show resolvable excesses in ^{26}Mg and isochron regressions yield initial ^{26}Al/^{27}Al ratios of type II chondrules that range from $(3.62 \pm 0.86) \times 10^{-6}$ to $(9.3 \pm 1.1) \times 10^{-6}$, which translates to formation ages between 2.71 $^{-0.22/+0.28}$ Ma and 1.75 $^{-0.11/+0.12}$ Ma after CAI. This overall range is indistinguishable from that determined for type I chondrules in Acfer 094. The initial ^{26}Al/^{27}Al ratio of the oldest type II chondrule is resolved from that of all other type II chondrules in Acfer 094. Importantly, the oldest type I chondrule and the oldest type II chondrule in Acfer 094 possess within analytical error indistinguishable initial ^{26}Al/^{27}Al ratios and Δ^{17}O values of ~0‰. Ages and oxygen isotope ratios clearly set these two chondrules apart from all other chondrules in Acfer 094. It is therefore conceivable that the formation region of these two chondrules differs from that of other chondrules and in turn suggests that Acfer 094 contains two distinct chondrule generations.

1. Introduction

Chondrules, ubiquitous in most chondritic meteorites, are spherical, igneous objects produced by heating events in the protoplanetary disk (e.g., Hewins, 1996; Brearley and Jones, 1998; Scott and Krot, 2007). The timing of chondrule formation is investigated by ^{26}Al-^{26}Mg chronometry that relies on the estimation of the initial ^{26}Al/^{27}Al ratios at the time of chondrule formation from the abundances of radiogenic (excess) ^{26}Mg produced by *in-situ* decay of the short-lived nuclide ^{26}Al (half-life: 0.705 Ma; Norris et al. 1983; Kita and Ushikubo 2012). The internal isochron method is applied to chondrules by analyzing the Al-Mg systematics of phases with high and low Al/Mg ratios, such as plagioclase and olivine or pyroxene, respectively. By this method, the range of formation ages among chondrules within a single meteorite can be determined at a precision as good as 0.1 Ma (e.g., Kita and Ushikubo, 2012, and references therein; Villeneuve et al., 2009; Pape et al., 2019). The formation ages of chondrules are usually expressed relative to that of Ca, Al-rich inclusions (CAIs), which are the oldest solid objects in the Solar System (e.g. Connelly et al. 2012), assuming that ^{26}Al was homogeneously distributed in the nascent solar nebula at canonical levels (5.2×10^{-5}, Jacobsen et al., 2008). Several studies have estimated the range of chondrule ages, for instance, for unequilibrated ordinary chondrites (e.g., Hutcheon and Hutchison, 1989; Russell et al., 1996; Kita et al., 2000; Huss et al., 2001; Mostefaoui et al., 2002; Rudraswami et al., 2008); CV (Srinivasan et al., 2000; Hutcheon et al., 2009; Nagashima et al., 2016) and CR chondrites (Nagashima et al., 2014; Schrader et al., 2017); the CO chondrite Yamato 81020 (Yurimoto and Wasson, 2002; Kunihiro et al., 2004; Kurahashi et al., 2008); and the ungrouped carbonaceous chondrite Acfer 094 (Sugiura and Krot, 2007; Ushikubo et al., 2013). According to these studies, chondrule formation ages range from ~1 to ~3 Ma after CAI (e.g., Kita and

Ushikubo, 2012), except for CR chondrites where most chondrules are younger than 3-4 Ma after CAI (Nagashima et al., 2014; Tenner et al., 2015a; Schrader et al., 2017).

Variations in chondrule ages within single chondrites are of particular interest because the onset and termination of chondrule formation would place some constraints on the extent of radial mixing in the proto-planetary disk as well as on the timing of parent body formation (e.g., Cuzzi et al., 2010; Kita and Ushikubo, 2012; Alexander and Ebel, 2012). Analysis of type I (FeO-poor) chondrules in Acfer 094 and Yamato 81020 (Y-81020) show narrow age ranges that are comparable to the analytical uncertainties (Acfer 094: 2.25 ± 0.25 Ma, 1SD, n=9; Y-81020: 2.02 ± 0.23 Ma, 1SD, n=14), but some chondrules possess resolvable ages relative to other chondrules of the same meteorite (Δt): $\Delta t = 0.8^{+0.4}_{-0.5}$ Ma in Y-81020 and $\Delta t = 0.6^{+0.3}_{-0.5}$ Ma in Acfer 094 (Kita and Ushikubo, 2012). On average, the ages of type II (FeO-rich) chondrules in Y-81020 (2.26 ± 0.36 Ma, 1SD, n=6; Kita and Ushikubo, 2012) are indistinguishable from those of type I chondrules, though some of them show lower initial $^{26}Al/^{27}Al$ ratios compared to those of most of the type I (FeO-poor) chondrules (Kunihiro et al., 2004; Kurahashi et al., 2008). This results in uncertainty in the actual age range that needs to be addressed since evaluation of radial mixing is highly dependent on the residence time of free-floating chondrules in the disk (Cuzzi et al., 2010).

In contrast to data from Ca-rich plagioclase in type I chondrules, type II chondrule data were obtained from Na-rich plagioclase, in which Mg self-diffusion is significantly faster (Costa et al., 2003; van Orman et al., 2014). Since Y-81020 experienced low-degree thermal metamorphism in its parent body with estimated peak temperatures ranging from 400 to 560 °C (type 3.05, Kimura et al., 2008), younger ages estimated for some type II chondrules could be the result of disturbance of the Al-Mg isotope system (e.g., Alexander and Ebel, 2012). Here we examine the Al-Mg system of chondrules of the ungrouped carbonaceous chondrite Acfer 094 (C3.00), which was only

minimally affected by parent body thermal metamorphism and aqueous alteration (Greshake, 1997; Grossman and Brearley, 2005; Busemann et al., 2007; Kimura et al., 2008), so that FeO-rich chondrules in this meteorite could have stayed closed with respect to the Al-Mg isotope system since their formation. Despite being an ungrouped chondrite, Acfer 094 shows chemical and mineralogical similarities to CO chondrites in terms of oxygen isotope ratios and modal abundance of chondrite components (Newton et al., 1995; Greshake, 1997; Weisberg et al., 2006). We will therefore compare results from Acfer 094 chondrules with those from the CO chondrite Y-81020.

Ushikubo et al. (2013) previously reported results from 10 type I chondrules from Acfer 094 with initial $^{26}Al/^{27}Al$ ratios ranging from $(4.2 \pm 2.0) \times 10^{-6}$ to $(9.0 \pm 1.5) \times 10^{-6}$. As discussed in Kita and Ushikubo (2012), the highest and lowest initial $^{26}Al/^{27}Al$ ratios of these chondrules are resolved, but 9 out of 10 chondrules show a narrow range of initial $^{26}Al/^{27}Al$ ratios that are indistinguishable within analytical uncertainties. Chondrules in Acfer 094 show a wide range of oxygen isotope ratios; $\Delta^{17}O$ ($= \delta^{17}O - 0.52 \times \delta^{18}O$) values of ~ –5‰ and ~ –2‰ are predominant (Ushikubo et al., 2012). No obvious correlations between initial $^{26}Al/^{27}Al$ ratios and $\Delta^{17}O$ values have been observed. However, it is noteworthy that the object with the highest $^{26}Al/^{27}Al$ ratio, i.e., the oldest object in the study of Ushikubo et al. (2013), is a type I-chondrule fragment (G39) with a $\Delta^{17}O$ value of ~ 0‰ (Ushikubo et al., 2012; 2013). Initial $^{26}Al/^{27}Al$ ratios and oxygen isotope ratios of this fragment will be discussed in great detail in the discussion section in conjunction with newly acquired data for type II chondrules.

We used a secondary ion mass spectrometer (SIMS) IMS 1280 that was upgraded with a RF (radio frequency) Plasma oxygen ion source to perform Al-Mg analyses of type II chondrules in Acfer 094. With the high-brightness oxygen primary ion beam, analysis of small plagioclase grains (<10 μm) in chondrule mesostasis was possible. The aim of this study is to compare initial

106 $^{26}Al/^{27}Al$ ratios of type I and II chondrules and to determine the age range recorded in a
107 representative subset of chondrules in one of the least thermally metamorphosed carbonaceous
108 chondrites. Complementing the study of Ushikubo et al. (2012), we obtained oxygen isotope ratios
109 of 9 type II chondrules to be able to identify chondrules with distinct initial $^{26}Al/^{27}Al$ ratios and
110 $\Delta^{17}O$ values. This might point to the presence of different chondrule generations within Acfer 094
111 and may help to further narrow down a maximum age range for chondrules in this chondrite.
112

2. Analytical Procedures

2.1 Procedures in preparation for isotope analyses

The section of Acfer 094 (USNM 7233-8), allocated from the Smithsonian Institution, National Museum of Natural History, was imaged previously by back-scattered (BSE) and secondary (SE) electron techniques (Ushikubo et al., 2012). Based on these images, type II chondrules suitable for Al-Mg isotope analyses were selected and the mineral chemistries of their plagioclase and olivine were analyzed using a Cameca SXFive electron microprobe (EPMA) located at the Department of Geoscience, UW-Madison (2 μm beam, 15kV; 20 nA for olivine, 10 nA for plagioclase). The EPMA analyses are reported together with mean detection limits of the measured oxides in Appendix EA 1. After selecting individual plagioclase grains for Al-Mg analysis, potential SIMS spot locations were imaged again by standard SEM techniques (Hitachi S-3400N, UW-Madison) to check for inclusions and cracks. Further, representative plagioclase grains from all dated chondrules were investigated by micro-Raman (JASCO NRS 1000, National Institute of Polar Research, Tokyo) in order to confirm their crystallinity. The acquisition time was 30 s. For each region analyzed, a Raman spectrum was acquired in the spectral region of 150 cm^{-1} to 1380 cm^{-1}.

Plagioclase grains in chondrule mesostasis that were selected for SIMS analysis had their locations marked by a focused ion beam (FIB) technique similar to the method described in Nakashima et al. (2012). For this task, we utilized two different field emission (FE) SEMs equipped with FIB systems located at the Materials Science Center, University of Wisconsin-Madison. We first used the FIB FEI Helios PFIB G4 to mark the locations with thin platinum films (3×3 μm^2, ~50nm thickness) deposited on the carbon-coated surfaces of the plagioclase grains, guided by SE images of the sample. The platinum films were easily recognizable in the SE images

produced by the FIB-SEM. Subsequently, 1x1 μm^2 square areas at the centers of the platinum depositions were removed along with the underlying carbon coatings (Fig. 1). This was performed using the FIB Zeiss Auriga, following procedures described in Defouilloy et al. (2017). The FIB marks are visible by SIMS ^{27}Al-ion imaging and allow for precise aiming of the primary ion beam (Nakashima et al., 2015) in combination with the NanoDeflector (Defouilloy et al., 2017) and high-resolution SE images of marked areas.

2.2 Oxygen three-isotope analysis of chondrule olivine

The oxygen three-isotope analyses of chondrule olivine were carried out using the Cameca IMS 1280 SIMS at the University of Wisconsin-Madison using multi-collector Faraday cups (Kita et al., 2010; Tenner et al., 2013; 2015b). The primary Cs^+ ion beam was focused to a ~10 µm diameter at ~2.5 nA producing secondary $^{16}O^-$ ion intensities of ~3×10^9 counts per second (cps). The external reproducibility of a San Carlos (SC) olivine standard ($\delta^{18}O$ = 5.32‰ VSMOW; Kita et al., 2010) was typically 0.2‰, 0.4‰, and 0.4‰ (2SD) for $\delta^{18}O$, $\delta^{17}O$, and $\Delta^{17}O$, respectively. Additional olivine standards (Fo_{60} and $Fo_{0.6}$) that cover the composition of olivine in type II chondrules in Acfer 094 were analyzed to calibrate the instrumental biases of the unknowns. Each SIMS pit was imaged after analysis to check for pit imperfections that might compromise the measured oxygen isotope ratios. More detailed information about SIMS oxygen isotope analysis and the calculation of mean chondrule oxygen isotope ratios, including related uncertainties, can be found in the Appendix EA 2.

2.3 Magnesium isotope analyses

The Al-Mg isotope analyses of plagioclase, as well as olivine and pyroxene, were performed in two separate sessions utilizing the Cameca IMS 1280 SIMS. The analytical conditions are

158 generally similar to those described in Ushikubo et al. (2013) except for the primary beam
159 conditions and the use of the multicollection electron multipliers for plagioclase analyses. For this
160 study, we used the RF plasma ion source that provides a higher primary-ion brightness than the
161 conventional Duoplasmatron source. In particular, a primary O_2^- beam was used because the
162 secondary ionization efficiency of Mg is higher with O_2^- primary ions than with O^- ions (Kita et
163 al., 2000). After analysis, each SIMS pit was imaged by standard SEM techniques to check pit
164 quality. The data reduction procedures for Al-Mg analyses follow those of Ushikubo et al. (2017).
165 Absolute Mg isotope ratios from Catanzaro et al. (1966), $^{25}Mg/^{24}Mg = 0.12663$ and $^{26}Mg/^{24}Mg =$
166 0.13932, were used for normalizing raw-measured Mg isotope ratios in delta-notations, $\delta^{25}Mg_m$
167 and $\delta^{26}Mg_m$, respectively. The instrumental biases were calibrated by analyses of several mineral
168 standards that generally cover the compositions of the unknowns. We assume a power function for
169 both natural and instrumental mass dependent fractionation, with the same power for convenience.
170 The excess $\delta^{26}Mg^*$, corresponding to the fraction of ^{26}Mg that formed by the decay of ^{26}Al in the
171 unknowns, is expressed as a function of the instrumental bias corrected $\delta^{25}Mg$ and $\delta^{26}Mg$ values:

172 $$\delta^{26}Mg^* = \left[\left(1+\frac{\delta^{26}Mg}{1000}\right) - \left(1+\frac{\delta^{25}Mg}{1000}\right)^{\frac{1}{\beta}}\right] \times 1000 \quad (1)$$

173 $$= \Delta^{26}Mg \times \left(1+\frac{\delta^{25}Mg}{1000}\right)^{\frac{1}{\beta}}$$

174 Where $\Delta^{26}Mg$ is the mass independent fractionation term and β is the power of the mass
175 fractionation law that is assumed to be 0.5128 (Davis et al., 2015). The term $\Delta^{26}Mg$ is identical to
176 (excess) $\delta^{26}Mg^*$ when the natural mass fractionation measured as $\delta^{25}Mg$ equals zero (see Ushikubo
177 et al., 2017).

178 *2.3.1 Multicollection electron multiplier analysis of plagioclase*

179 Plagioclase was analyzed for Al and Mg isotopes by a critically illuminated primary beam of
180 approximately 3 µm diameter at 50 pA intensity. If the area available for analysis was large
181 enough, this beam was rastered by 3 × 3 µm to form a ~5 µm rectangular spot. For relatively small
182 plagioclase grains, smaller raster sizes of 1 × 1 µm were applied that resulted in more roundish ~4
183 µm spots. Secondary $^{24}Mg^{+}$, $^{25}Mg^{+}$, $^{26}Mg^{+}$ ions were detected simultaneously using three electron
184 multipliers (EM); 2 miniature ones (manufactured by Hamamatsu) on the multi-collection detector
185 array for $^{24}Mg^{+}$, $^{25}Mg^{+}$ and another (manufactured by ETP) on the axial detector for $^{26}Mg^{+}$. The
186 mass resolving power was set to ~2,000 (at 10% valley) on all three EM detectors by using exit
187 slit widths of ~500 µm (Slit #1 for the multi-collection array and adjustable slit for axial detector).
188 Under these conditions, the $^{48}Ca^{2+}$ and $^{24}MgH^{+}$ interferences are less than 10^{-4} of the $^{24}Mg^{+}$ and
189 $^{25}Mg^{+}$ signals, respectively (see mass spectrum in Appendix EA 8). The $^{27}Al^{+}$ ions were detected
190 on the axial FC by peak switching. The secondary intensity of $^{24}Mg^{+}$ was typically ~ 2×10^{4} cps
191 (counts per seconds) for the plagioclase standard with 0.11 wt.% MgO. The analyses last for 50
192 min., including 60 cycles of magnetic field switching for detection of Mg (40s) or Al (3s) isotopes.
193 To maintain constant relative gains among the three EM detectors, an automated high voltage
194 adjustment routine was applied at the beginning of each analyses (see Appendix EA 2).

195 We used a natural plagioclase mineral standard ("Lab1" An_{59}, MgO: 0.11 wt.%, Kita et al.,
196 2012) for instrumental bias correction of the Mg isotope ratios and the relative sensitivity factor
197 of $^{27}Al/^{24}Mg$. The $\delta^{25}Mg$ and $\delta^{26}Mg$ values of the plagioclase standard are assumed to be 0‰ on
198 the DSM-3 scale. The relative sensitivity factor

199 $$RSF = (^{27}Al/^{24}Mg)^{SIMS}_{Measured} / (^{27}Al/^{24}Mg)^{EPMA}_{True} \quad (2)$$

was derived from the bracketing standard analyses employing a $(^{27}Al/^{24}Mg)^{EPMA}_{True}$ ratio of 278 (±6%, Kita et al., 2012). Uncertainties in $^{27}Al/^{24}Mg$ ratios were propagated from the in-run variation of individual analyses (2SE%), the external reproducibility of the bracketing standard analyses (2SD%), and uncertainty in the $(^{27}Al/^{24}Mg)^{EPMA}_{True}$ (6%). Since there was no appreciable difference in the RSF between An_{59} and An_{100}, we used the same RSF for plagioclase with higher Na compositions ($An_{<30}$), although an uncertainty of 10% (instead of 6%) was applied in these cases for safety. The external reproducibility of the SIMS ($^{27}Al/^{24}Mg$) analyses of the Lab1 plagioclase standard was better than 5% (2SD). Ideally, analyses comprised 60 cycles (50 min) but frequently the analyses had to be stopped when the secondary $^{24}Mg^+$ beam increased to $>10^5$ cps because the primary beam sputtered other Mg-rich minerals such as olivine or pyroxene. In these cases, the first N cycles reflecting only the signal from plagioclase were included in the data reduction; correspondingly, only the first N cycles of the running standards were considered for correction of these specific isotope ratios. Further information regarding magnesium isotope analysis protocol and conditions are compiled in Appendix EA 2.

2.3.2 Multicollection Faraday cup analysis of olivine and pyroxene

Olivine and pyroxene were analyzed for their Al-Mg isotope systematics using an O^{2-} primary beam with a spot size of 7 µm at 1nA intensity. The ions of three Mg isotopes and $^{27}Al^+$ ions were detected using four FCs on the multi-collection detector array (Ushikubo et al., 2013; 2017). The duration of a single analysis was 6 min. The secondary intensity of $^{24}Mg^+$ on the SC olivine standard was typically ~ 2×10^8 cps. For olivine analyses, SC olivine (Fo_{89}) was chosen as the running standard and, to calibrate instrumental bias, two additional olivine standards (Fo_{100}, Fo_{60}) with known $\delta^{25}Mg$ and $\delta^{26}Mg$ values on the DSM-3 scale (Kita et al., 2016) were measured ($\delta^{25}Mg_{DSM3}$ of Fo_{100}, Fo_{89}, Fo_{60}: –0.366‰, –0.072‰, –0.013‰, respectively). Pyroxene analyses

were bracketed by an enstatite standard (En_{85}) with known Mg isotope ratios on the DSM-3 scale ($\delta^{25}Mg_{DSM3}$ = –0.257‰); the chemical composition of the standard is similar to that of the unknowns. The difference between the raw-measured $\delta^{25}Mg_m$ values and the corrected $\delta^{25}Mg$ values in DSM-3 scale range from –3.3‰ to –1.3‰ for the olivine standards and +1.1‰ for the enstatite standard during one SIMS session. The typical external reproducibility of raw-measured $\delta^{25}Mg_m$ and $\Delta^{26}Mg_m^*$ for olivine and pyroxene standards were better than 0.1‰. However, Ushikubo et al. (2017) found that there is an expected additional variability of ~0.2‰ in raw-measured $\delta^{25}Mg_m$ of the San Carlos olivine standard when it was analyzed in different SIMS mounts. The uncertainties in the $\delta^{25}Mg$ values of chondrule olivine and pyroxene are therefore at least 0.2‰ and likely larger because of the limited number of standards used in this study. Additionally, we corrected the $\delta^{25}Mg$ values for effects of sample topography (see Appendix EA2) which further increases the uncertainty in $\delta^{25}Mg$ values of olivine in chondrules.

2.4 Isochron regression

Isochron regressions were performed using the "Model 1" fit of the Isoplot 4.15 macro collection (Ludwig, 2008). However, if the "Probability of Fit" was below 5%, the "Robust regression" algorithm was chosen instead. The "Probability of Fit" represents the likelihood that the estimated scatter of points from a line (as expected from the analytical uncertainties) exceeds the amount of actually observed scatter of the data points (Ludwig, 2008). Since the uncertainty in the $(^{27}Al/^{24}Mg)^{EPMA}_{True}$ is a systematic source of error that applies to all analyses and doesn't contribute to the scatter from an isochron, regressions were made ignoring the 6% or 10% uncertainty in the $^{27}Al/^{24}Mg$ ratios. Uncertainties in initial $^{26}Al/^{27}Al$ ratios and initial $\delta^{26}Mg^*_0$ are 95%-confidence intervals. Data used for isochron regression and information about which regression model was used can be found in the Appendix EA6.

3. Results

We obtained oxygen isotope ratios for 9 type II chondrules from the Acfer 094 USNM 7233-6 thin section, including three chondrules that were chosen for Al-Mg isotope analyses. Ushikubo et al. (2012) previously reported the oxygen isotope ratios of 12 FeO-rich chondrules from the same section, of which four chondrules were chosen for Al-Mg isotope analyses in this work. The seven chondrules analyzed for Al-Mg systematics were chosen on the basis of the presence of plagioclase grains larger than 5 μm in size.

The data obtained during this study are documented and presented in detail in the following way: the mineral compositions of plagioclase are given in Appendix EA 1; Appendix EA 3 contains the oxygen-three isotope data set; Appendix EA 4 oxygen three-isotope diagrams for each of the 9 analyzed chondrules; Appendix EA 5 documents the positions of the SIMS measurements; The magnesium isotope data set and isochron calculations are provided in Appendix EA 6; documentation for the magnesium isotope measurement positions in Appendix EA 7. Additional figures concerning the magnesium isotope characteristics and a typical mass spectrum are provided in Appendix EA 8. Appendix EA 9 contains a BSE mosaic of the Acfer 094 USNM 7233-6 thin section.

3.1 Petrography of FeO-rich chondrules and mineral chemistry

Figure 2 shows BSE images of the 7 plagioclase-bearing, porphyritic, type II chondrules (150 - 300 μm) dated by ^{26}Al-^{26}Mg chronometry, including six olivine-rich (type IIA, Fig. 2a-d and f-g) chondrules and one pyroxene-rich (type IIB, Fig. 2e) chondrule. The large olivine phenocrysts are almost always normally zoned with respect to Mg#, i.e., rims are more FeO-rich than cores; the large phenocryst in chondrule G9 exhibits a faint oscillating zoning (Fig. 2a). Olivine grains in

several chondrules (e.g., G10, Fig. 2b) possess forsterite-rich cores indicative for relict olivine. Excluding these forsterite-rich cores, the mean chondrule Mg#s range from 48 to 70 (see Table 1). The type IIB chondrule G85 is mainly comprised of low-Ca ($En_{86}Fs_{13}Wo_{1}$; Mg#: 87; Table 1) and high-Ca ($En_{61}Fs_{10}Wo_{29}$) pyroxene, with the latter forming overgrowths on the low-Ca pyroxenes (Fig. 2e). Chromite is a common additional mineral in type II chondrules from Acfer 094 and contains 9-19 wt.% Al_2O_3 and 4-8 wt.% MgO.

The chondrule mesostasis shows no evidence for hydrous alteration or formation of secondary minerals. The mesostasis of dated chondrules contains plagioclase in combination with high-Ca pyroxenes, as shown in Fig. 3. Plagioclase was identified from the typical Raman peaks at 505, 485, 402, and 280 cm^{-1}. The Raman spectra show that none of the plagioclase grains are high-temperature polymorphs, such as dmisteinbergite and kumdykolite. In chondrule G63, anorthitic glass ($An_{\sim 40}$) is the main constituent of mesostasis, but small patches of plagioclase that were large enough for analysis were observed at the chondrule margin (Fig. 1, 2d, 3e). Plagioclase in chondrule G85 contains abundant small crystallites of presumably high-Ca pyroxene (Fig. 3f, g). On average, the anorthite contents of the plagioclase in the dated chondrules range from An_{15} to An_{54} (Table 1). Chondrules G9 and G85 possess the most albite-rich compositions of up to An_{8} and An_{13}, respectively. The variability of plagioclase compositions within individual chondrules indicates zoning of plagioclase with respect to anorthite content. The mean K-feldspar content of plagioclase grains for individual chondrules ranges from 0.4 mol.% to 2.4 mol.% and broadly correlates with albite content.

The chondrules that were analyzed for oxygen isotopes are shown in Appendix EA 5; three of them (G9, G61, G108) were also analyzed for Al-Mg systematics. All chondrules are porphyritic

and olivine-rich (IIA), with mean Mg#s between 52 and 71. Chondrules G25, G88, and G120 contain glassy mesostasis; the mesostases of the other chondrules comprise plagioclase.

3.2 Oxygen isotope ratios of chondrule olivine

Most olivine analyses plot on the Primitive Chondrule Minerals (PCM, Ushikubo et al., 2012) line or between PCM and CCAM (Carbonaceous Chondrite Anhydrous Minerals, Clayton et al., 1977) lines (Appendix EA 4). The $\delta^{18}O$ values of individual olivine analyses range from –1.9‰ to +2.7‰ and the $\delta^{17}O$ values are in between –4.8‰ and –0.5‰ ($\Delta^{17}O$: –3.9 to –1.8‰), excluding two ^{16}O-rich analyses from chondrule G120 ($\delta^{18}O$: –36.95‰, –8.69‰). Three of 8 chondrules contain isotopic relict olivine grains (Fig. 4) that were identified by the method described in Appendix EA 2. The mean chondrule $\delta^{17}O$, $\delta^{18}O$, and $\Delta^{17}O$ values are calculated by using multiple analyses from a single chondrule that are indistinguishable from each other, based on a calculation scheme (see Appendix EA 2; more details in Ushikubo et al., 2012; Tenner et al., 2013; Hertwig et al., 2018). The mean chondrule $\Delta^{17}O$ values fall in the range of –3.6‰ to –2.1‰ (Table 2; Fig. 4, 5). For chondrule G99, it was not possible to calculate a mean $\Delta^{17}O$ value because the analyses form two clearly resolvable clusters in the oxygen three-isotope diagram; the Mg#s of olivine grains are variable (Mg#: 56-67) but do not indicate the presence of relict grains in either of both clusters.

3.3 The ^{26}Al-^{26}Mg systematics of chondrules

The $^{27}Al/^{24}Mg$ ratios obtained by analysis of the plagioclase grains range mainly from 150 to 300, but two chondrules (G9, G85) comprise plagioclase with $^{27}Al/^{24}Mg$ ratios higher than 500 and up to 1700 (Table 3). All but one plagioclase analysis show resolvable $\delta^{26}Mg^*$ with values higher than 10‰ and as high as 31‰ and 112‰ in chondrules G9 and G85, respectively. The

olivine and pyroxene analyses yield normal $\delta^{26}Mg^*$ values to within the analytical uncertainties, except for 3 analyses with marginally resolvable negative $\delta^{26}Mg^*$ values (–0.09 ±0.08‰, –0.11 ±0.08‰, –0.14 ±0.06‰). There is no significant variability of $\delta^{25}Mg$ values in plagioclase within the analytical errors (2-4‰). There are only small deviations (≤0.5‰) from normal in the $\delta^{25}Mg$ values of the olivine and pyroxene analyses, possibly due to inaccuracies of the calibrations that were based on only a limited number of olivine and pyroxene standards. Further, these standards are located on separate SIMS mounts and not on the Acfer 094 thin section which could be the cause for additional variations in the $\delta^{25}Mg$ values.

The initial $^{26}Al/^{27}Al$ ratios (Table 4, Fig. 6) inferred from the isochron regressions of 6 out of 7 chondrules range from $(3.62 \pm 0.86) \times 10^{-6}$ to $(5.22 \pm 0.87) \times 10^{-6}$ corresponding to chondrule ages between $2.71^{-0.22/+0.28}$ Ma and $2.34^{-0.16/+0.18}$ Ma after CAI formation, based on a canonical $(^{26}Al/^{27}Al)_0$ of 5.2×10^{-5}. None of these chondrule ages are resolvable from one another. Only the analysis of chondrule G85 yields a significantly higher initial $^{26}Al/^{27}Al$ ratio of $(9.3 \pm 1.1) \times 10^{-6}$ that corresponds to an ^{26}Al age of $1.75^{-0.11/+0.12}$ Ma after CAI formation. The difference in initial $^{26}Al/^{27}Al$ ratios of chondrule G85 and the next oldest chondrule, G61 with $(^{26}Al/^{27}Al)_0 = (5.22 \pm 0.87) \times 10^{-6}$, translates to a resolvable age difference of $0.59^{+0.29/-0.28}$ Ma. The calculated age difference between chondrules G9 and G85 is $0.91^{+0.26/-0.25}$ Ma, taking into account the 10% uncertainty associated with the RSF of Na-rich plagioclase in both chondrules. Finally, the age difference between the chondrule G86 and G85, i.e., the maximal age difference between two type II chondrules in this data set, is $0.96^{+0.39/-0.34}$.

The initial $^{26}Al/^{27}Al$ ratios are not correlated with the anorthite content of the plagioclase in the chondrules; there is also no correlation between the $(^{26}Al/^{27}Al)_0$ and the Mg# of the chondrules (see Appendix EA 8). The initial $\delta^{26}Mg^*_0$ values defined by the isochron intercepts vary between

335 –0.043 ± 0.040‰ and –0.004 ± 0.046‰ for Model 1 fits. For one chondrule (G108), the robust

336 regression was applied, and the $\delta^{26}Mg^{*}_{0}$ values are less precisely defined (–0.14 +0.15/–1.4‰).

337

4. Discussion

4.1 Ranges of initial $^{26}Al/^{27}Al$ ratios of type I and II chondrules in Acfer 094

Ushikubo et al. (2013) reported initial $^{26}Al/^{27}Al$ ratios for type I chondrules in Acfer 094 ranging from $(4.2 \pm 2.0) \times 10^{-6}$ to $(9.0 \pm 1.5) \times 10^{-6}$ (Fig. 7a, Table 5). Within the analytical uncertainties, this range is indistinguishable from that observed in the type II chondrules whose initial $^{26}Al/^{27}Al$ ratios vary between $(3.62 \pm 0.86) \times 10^{-6}$ and $(9.3 \pm 1.1) \times 10^{-6}$. Concurrent formation of type I and II chondrules in Acfer 094 contrasts with findings from Y-81020 where some type II chondrules are younger than type I chondrules (Fig. 7b) (Kunihiro et al., 2004; Kurahashi et al., 2008). Therefore, a suggested gradual change in redox conditions from reducing to more oxidizing conditions (Kurahashi et al., 2008) cannot be confirmed by data from Acfer 094 at this point. We note that the three youngest Acfer 094 chondrules in Fig. 7a are type II chondrules. However, whether there is a systematic difference in chondrule ages between type I and II chondrules requires improvements in the precision of the initial $(^{26}Al/^{27}Al)_0$ for type I chondrules in Acfer 094.

4.2 Undisturbed Al-Mg system in albite-rich plagioclase in Acfer 094 chondrules

Albite-rich plagioclase is generally more susceptible to Mg diffusion than anorthite (e.g., Costa et al., 2003; van Orman et al., 2014). Based on an experimental investigation of Mg self-diffusion in plagioclase of varying anorthite contents, van Orman et al. (2014) calculated the heating times needed for loss of half of the excess ^{26}Mg in plagioclase. For instance, at 500 °C, loss of half of excess ^{26}Mg would occur after 30 ka to 200 ka in a plagioclase sphere (25 μm diameter) with an albite-rich composition (An_{20} to An_{40}). This would result in an apparently younger ^{26}Al-age that was reset by 0.705 Ma years, the half-life of ^{26}Al. Although the evidence of

360 thermal metamorphism in Acfer 094 is minimal (Greshake, 1997; Grossman and Brearley, 2005;
361 Busemann et al., 2007; Kimura et al., 2008), this does not guarantee that the chondrule plagioclase
362 stayed closed with respect to radiogenic ^{26}Mg since crystallization from the melt.

363 In most Acfer 094 chondrules, the MgO contents of plagioclase are relatively homogeneous
364 within each chondrule leading to a narrow range of $^{27}Al/^{24}Mg$ values (Fig. 6a-e). In contrast, the
365 MgO contents of Na-rich plagioclase in chondrules G9 and G85 are extremely low (<0.1wt.%)
366 and variable (Fig. 6f). Moreover, a few analyses exhibit significant internal variability of $^{27}Al/^{24}Mg$
367 ratios as shown in Fig. 8. In this specific analysis (G9: 3 Plag), the ^{27}Al signal varies with depth in
368 a way that is consistent with that of the plagioclase standards (Fig. 8a), whereas the $^{27}Al/^{24}Mg$
369 ratios abruptly fall from 1000 to 300 over two cycles approximately halfway through the analysis
370 (Fig. 8b); this change is accompanied by a drop in the raw $\delta^{26}Mg_m$ values without any correlated
371 changes in the raw $\delta^{25}Mg_m$ values (Fig. 8c). Because of the abrupt decrease in $^{27}Al/^{24}Mg$ ratios,
372 the data reduction only considered cycles 1 to 36 (Table 3). A plagioclase analysis ideally consists
373 of 60 cycles collected over a depth profile of approximately 4 μm (SIMS pit depth), i.e., one
374 analytical cycle integrates the composition of material that is ~70 nm thick. The sharp drop in raw
375 $\delta^{26}Mg$ over the course of just two cycles, or 140 nm, demonstrates that only very limited diffusive
376 Mg exchange between plagioclase domains occurred. Further, data reduction based only on cycles
377 41 - 60, the second homogeneous portion of the analysis, results in values for $\delta^{26}Mg^*$ and
378 $^{27}Al/^{24}Mg$ that plot on the internal chondrule isochron of G9 (Fig. 8d). This confirms that
379 plagioclase domains retained their different levels of excess ^{26}Mg in one of the most albite-rich
380 plagioclase ($An_{\sim 15}$, EA 1) investigated in this study.

4.3 Two generations of chondrules with distinct oxygen isotopes and formation ages

This section discusses the newly obtained data on type II chondrules in combination with pre-existing data on type I chondrules (Ushikubo et al., 2012, 2013); Table 5 summarizes the relevant information. Most of the variability in ages of type I and II chondrule can be attributed to the two oldest chondrules G39 and G85, both of which show similarities in their oxygen isotopes that differentiate them from all the other chondrules so far analyzed from Acfer 094. The mean chondrule Mg#s of G39 and G85 are intermediate between typical FeO-poor or FeO-rich chondrules in carbonaceous chondrites; i.e., fragment G39 is FeO-rich (Mg# ~ 92) in comparison to typical type I chondrules and chondrule G85 is FeO-poor (Mg# ~ 87) in comparison to other type II chondrules with Mg#s of typically <70 (Fig. 5). Further, chondrule fragment G39 and chondrule G85 have $\Delta_{17}O$ values of ~0‰ (Fig. 9) and, more importantly, their $\delta_{18}O$ values are fractionated in such a way that ratios plot off the PCM line (Ushikubo et al., 2012). The PCM line is interpreted to be a mixing line between $_{16}O$-rich and $_{16}O$-poor reservoirs. Deviation from such a mixing line points to chondrule precursor material that records different, slightly fractionated oxygen isotope ratios (e.g., Clayton et al., 1983; Kita et al., 2010; Tenner et al., 2017); in Acfer 094, this fractionated reservoir is only reflected in the oldest chondrules G39 and G85.

Chondrules with oxygen isotope ratios that plot above the PCM line and close to the TF line were reported for the Y-82094 ungrouped carbonaceous chondrite (Tenner et al., 2017) as well for the CV chondrites Kaba (Hertwig et al., 2018) and NWA 8613 (Hertwig et al., 2017). In the case of Y-82094, Tenner et al. (2017) combined evidence from oxygen isotopes and elevated Mn/Fe ratios of chondrule olivine to propose that "ordinary chondrite-like" precursor material was sampled by those chondrules. Tenner et al. (2017) note that, although oxygen isotope ratios of these chondrules resemble values from ordinary chondrites (OC), the $\Delta_{17}O$ values of OC type II

chondrules are typically higher than 0‰ (+0.5‰; e.g., Kita et al., 2010). For the specific chondrules in Kaba and NWA 8613, a similar conclusion cannot be easily drawn since they either lack primary olivine (Kaba) or olivine does not show elevated Mn/Fe ratios (NWA 8613) (Hertwig et al., 2017; 2018). Chondrule G85 from Acfer 094 is free of olivine, hence, it is not possible to evaluate the olivine mineral chemistry here. Olivine in G39 is zoned with respect to MnO contents (MnO: 0.1 – 0.4 wt.%), with low MnO contents in central areas making it difficult to unequivocally link this chondrule to OC chondrule-like precursors. However, in contrast to comparable chondrules in other carbonaceous chondrites, the formation ages of G39 and G85 in addition to fractionated oxygen isotope ratios, clearly set both chondrules apart from all other so far analyzed from Acfer 094.

The initial $^{26}Al/^{27}Al$ ratio of chondrule G85 [$(9.3 \pm 1.1) \times 10^{-6}$] is indistinguishable from that of G39 [$(9.0 \pm 1.5) \times 10^{-6}$, Ushikubo et al. (2013), see Table 5] but clearly resolvable from those of all analyzed type II chondrules with $\Delta^{17}O$ <0 ‰ (Figs. 7 and 9). The initial $^{26}Al/^{27}Al$ ratios of type I chondrules have larger uncertainties than those determined in the present study but, excluding G39, the $(^{26}Al/^{27}Al)_0$ of G85 is resolved from those of all type I chondrules but one [G73: $(7.6 \pm 1.8) \times 10^{-6}$, Ushikubo et al. (2013)]. Chondrule G73 is a typical type IAB chondrule with a high mean Mg# (~99) and low $\Delta^{17}O$ value of ~–6‰, hence, there is no indication that origin of chondrule G73 is linked to that of G39 and G85. In conclusion, we suggest that G39 and G85 belong to a different chondrule generation based on their significantly older ages and distinct oxygen isotopes. Excluding these older chondrules, the observed age range is $0.76^{+0.49}_{-0.49}$ Ma determined by considering G73 as the oldest and G86 as the youngest chondrule.

4.4. Implications for mixing processes in the protoplanetary disk

Using the terminology by Cuzzi et al. (2010), the specific chondrule ensemble contained in a single meteorite represents a grab sample of constituents present in the respective disk region. At the time and place the Acfer 094 parent body formed, there was a reservoir of material represented by chondrules G39 and G85 that formed 0.4 - 0.8 Ma before accretion. One possibility is to treat the age difference as the travel time of these chondrules from the place of their formation to the location of the accretion of their parent body. Radial mixing (e.g., Cuzzi et al., 2010), possibly enhanced by meridional flow of material close to the midplane (e.g., Desch et al., 2018), could have facilitated chondrule migration. Transport of precursor material or chondrules from, for instance, 2 AU to 4 AU within <1 Ma would be plausible in this context (Cuzzi et al., 2010). Another possibility is that chondrules formed closer to the region of the Acfer 094 parent body accretion. In this case, both chondrules had to be stored for 0.4 – 0.8 Ma without being affected by successive heating event, perhaps in a scenario similar to that proposed by Desch et al. (2018) for the storage of CAIs.

Excluding these older chondrules, the other chondrules sampled by the Acfer 094 parent body and analyzed here are indistinguishable with respect to formation age but belong either to the ^{16}O-rich ($\Delta^{17}O \sim -5‰$) or ^{16}O-poor ($\sim -2‰$) chondrule group (Fig. 9) (Ushikubo et al., 2012; 2013), i.e., chondrules formed in two different environments with respect to oxygen isotope ratios. In principle, these oxygen isotope reservoirs could have been spatially separated or they were separated in time; the latter is possible assuming that the change in effective oxygen isotope ratios of a specific disk location could have occurred in a shorter time span than what is currently resolvable. However, based on the presence of ^{16}O-poor relict grains in ^{16}O-rich chondrules and ^{16}O-rich relicts in relatively ^{16}O-poor chondrules, Ushikubo et al. (2013) suggested that the oxygen

isotope reservoirs were more likely separated in space rather than in time. This means that crystallization of type I and II chondrules could have occurred contemporaneously in neighboring disk regions. Since elevated chondrule $\Delta^{17}O$ values are thought to be mainly caused by enrichment of ^{16}O-poor water ice among chondrule precursors, it is conceivable that some type I chondrules and most type II chondrules formed close to the water condensation front, where high degrees of enrichment of water ice are to be expected (e.g., Cuzzi and Zahnle, 2004); precursors of the ^{16}O-rich type I chondrules, on the other hand, possibly contained a smaller amount of water ice and formed at a distance from this condensation front. Chondrules from both regions later mixed and got incorporated in the Acfer 094 parent body.

5. Conclusions

The ^{26}Al ages of 7 type II chondrules from one of the most pristine carbonaceous chondrite Acfer 094 (ungrouped, 3.00) were determined using the Cameca IMS 1280 in combination with a RF plasma ion source. Further, the oxygen isotopes of 9 type II chondrules were analyzed to complement existing oxygen isotope data (Ushikubo et al., 2012).

1) All analyzed chondrules contain plagioclase with resolvable excess ^{26}Mg. The range of initial $^{26}Al/^{27}Al$ ratios of type II chondrules is identical to the range of initial $^{26}Al/^{27}Al$ ratios obtained for type I chondrules in an earlier study (Ushikubo et al., 2013). Consequently, type II chondrules are not systematically younger than type I chondrules. Further, we demonstrated that there is no detectable alteration of pristine $(^{26}Al/^{27}Al)_0$ in the albitic plagioclase of Acfer 094 chondrules.

2) When excluding the oldest type II chondrule (IIB, G85; $1.75\ ^{-0.11}/_{+012}$ Ma), the initial $^{26}Al/^{27}Al$ ratios of type II chondrules correspond to formation ages between $2.71\ ^{-0.22}/_{+0.28}$ Ma and $2.34\ ^{-0.16}/_{+0.18}$ Ma after CAI. These ages are indistinguishable from each other and would be consistent with a formation age of ~2.4 Ma after CAI, if the chondrules formed during a single event.

3) The two oldest Acfer 094 chondrules [type IA fragment G39 (Ushikubo et al. 2013), type II G85] possess $\Delta^{17}O$ values of ~0‰ and isotope ratios that plot left of the PCM line in the oxygen three-isotope diagram. Chondrules with similar oxygen isotope ratios were described, for instance, in the Y-82094 ungrouped carbonaceous chondrite and it was speculated that they formed from "ordinary chondrite-like" precursors in the Y-81020 chondrule-forming region.

4) The age difference between the oldest chondrules (G39, G85) and the rest (~0.4 - 0.8 Ma) could be interpreted as transit time during which G39 and G85 traveled from their formation region

to the location of the Acfer 094 parent body accretion. Alternatively, if formed close to the location of later Acfer 094 accretion (no large-scale transport), both chondrules had to be stored for ~0.4 - 0.8 Ma and avoided reprocessing in the heating events that formed other type I and II chondrules.

Acknowledgments

We wish to thank Glenn MacPherson from the Smithsonian Institution for providing the Acfer 094 thin section, Michael Spicuzza for help with SIMS operation, John Fournelle and Bill Schneider for assistance with EPMA analysis and SEM imaging, and Richard Noll for operating FIB instruments. We also thank an anonymous reviewer and Conel Alexander for helpful reviews and Dimitri Papanastassiou for thoughtful editorial handling of this paper. This work is supported by NASA Emerging World Program (NNX17AE29G, N. K.) and a Grant-in-aids of Monkashou, Japan (No. 26400510 to M. K.). The upgrade of the RF plasma source is supported by the NASA Laboratory Analysis of Returned Samples and Planetary Major Equipment Programs (NNX16AG80G) and the NSF Instrumentation and Facility Program (EAR-1355590). WiscSIMS is partly supported by NSF (EAR-1658823). Support for FIB instrumentation was provided by the University of Wisconsin-Madison Office of the Vice Chancellor for Research and Graduate Education with funding from the Wisconsin Alumni Research Foundation, the College of Engineering, and the NSF Materials Research and Engineering Center (NSF DMR-1121288).

500 # References

501 Alexander C. M. O'D. and Ebel D. S. (2012) Questions, questions: Can the contradictions
502 between the petrologic, isotopic, thermodynamic, and astrophysical constraints on chondrule
503 formation be resolved? *Meteorit. Planet. Sci.* **47**, 1157–1175.

504 Brearley A. J. and Jones R. H. (1998) Chondritic Meteorites. *Rev. Mineral. Geochem.* **36**, 3-01 -
505 3-398.

506 Busemann H., Alexander C. M. O'D. and Nittler L. R. (2007) Characterization of insoluble
507 organic matter in primitive meteorites by microRaman spectroscopy. *Meteorit. Planet. Sci.*
508 **42**, 1387–1416.

509 Catanzaro E. J., Murphy T. J., Garner E. L., Shields W. R. (1966) Absolute isotopic abundance
510 ratios and atomic weight of magnesium. *J. Res. Natl. Bur. Stan. Sect. A*. **70A**, 453-458.

511 Clayton R. N., Onuma N., Grossman L. and Mayeda T. K. (1977) Distribution of the pre-Solar
512 component in Allende and other carbonaceous chondrites. *Earth Planet. Sci. Lett.* **34**, 209–
513 224.

514 Clayton R. N., Onuma N., Ikeda Y., Mayeda T. K., Hutcheon I. D., Olsen E. J. and Molini-
515 Velsko C. (1983) Oxygen isotopic compositions of chondrules in Allende and ordinary
516 chondrites. In *Chondrules and their origins* (ed. E. A. King). Lunar and Planetary Institute,
517 Huston, TX. pp. 37–43.

518 Costa F., Chakraborty S. and Dohmen R. (2003) Diffusion coupling between trace and major
519 elements and a model for calculation of magma residence times using plagioclase. *Geochim.*
520 *Cosmochim. Acta* **67**, 2189–2200.

Cuzzi J. N., Hogan R. C. and Bottke W. F. (2010) Towards initial mass functions for asteroids and Kuiper Belt Objects. *Icarus* **208**, 518–538.

Cuzzi J. N. and Zahnle K. J. (2004) Material Enhancement in Protoplanetary Nebulae by Particle Drift through Evaporation Fronts. *Astrophys. J.* **614**, 490–496.

Davis A. M., Richter F. M., Mendybaev R. A., Janney P. E., Wadhwa M. and McKeegan K. D. (2015) Isotopic mass fractionation laws for magnesium and their effects on ^{26}Al–^{26}Mg systematics in solar system materials. *Geochim. Cosmochim. Acta* **158**, 245–261.

Defouilloy C., Nakashima D., Joswiak D. J., Brownlee D. E., Tenner T. J. and Kita N. T. (2017) Origin of crystalline silicates from Comet 81P/Wild 2: Combined study on their oxygen isotopes and mineral chemistry. *Earth Planet. Sci. Lett.* **465**, 145–154.

Desch S. J., Kalyaan A. and Alexander C. M. O'D. (2018) The Effect of Jupiter's Formation on the Distribution of Refractory Elements and Inclusions in Meteorites. *Astrophys. J. Suppl. S.* **238**, 1–31.

Greshake A. (1997) The primitive matrix components of the unique carbonaceous chondrite Acfer 094: A TEM study. *Geochim. Cosmochim. Acta* **61**, 437–452.

Grossman J. N. and Brearley A. J. (2005) The onset of metamorphism in ordinary and carbonaceous chondrites. *Meteorit. Planet. Sci.* **40**, 87–122.

Hertwig A., Defouilloy C., Kimura M. and Kita N. T. (2017) Oxygen isotope systematics of chondrule minerals from the reduced CV3 chondrite NWA 8613. *Lunar Planet. Sci. XLVIII.* Lunar Planet. Inst., Houston, #1227(abstr.).

Hertwig A. T., Defouilloy C. and Kita N. T. (2018) Formation of chondrules in a moderately high dust enriched disk: Evidence from oxygen isotopes of chondrules from the Kaba CV3 chondrite. *Geochim. Cosmochim. Acta* **224**, 116–131.

Hewins R. H. (1996) Chondrules and the protoplanetary disk: an overview. In *Chondrules and the protoplanetary disk* (eds. R. H. Hewins, R. H. Jones and E. R. D. Scott). Cambridge Univ. Press, Cambridge. pp. 3–9.

Huss G. R., MacPherson G. J., Wasserburg G. J., Russel S. S. and Srinivasan G. (2001) Aluminum-26 in calcium-aluminum-rich inclusions and chondrules from unequilibrated ordinary chondrites. *Meteorit. Planet. Sci.* **36**, 975–997.

Hutcheon I. D. and Hutchison R. (1989) Evidence from Semarkona ordinary chondrite for ^{26}Al heating of small planets. *Nature* **337**, 238–241.

Hutcheon I. D., Marhas K. K., Krot A. N., Goswami J. N. and Jones R. H. (2009) ^{26}Al in plagioclase-rich chondrules in carbonaceous chondrites: Evidence for an extended duration of chondrule formation. *Geochim. Cosmochim. Acta* **73**, 5080–5099.

Jacobsen B., Yin Q.-Z., Moynier F., Amelin Y., Krot A. N., Nagashima K., Hutcheon I. D. and Palme H. (2008) ^{26}Al–^{26}Mg and ^{207}Pb–^{206}Pb systematics of Allende CAIs: Canonical solar initial ^{26}Al/^{27}Al ratio reinstated. *Earth Planet. Sci. Lett.* **272**, 353–364.

Kimura M., Grossman J. N. and Weisberg M. K. (2008) Fe-Ni metal in primitive chondrites: Indicators of classification and metamorphic conditions for ordinary and CO chondrites. *Meteorit. Planet. Sci.* **43**, 1161–1177.

561 Kimura M., Nakajima H., Hiyagon H. and Weisberg M. K. (2006) Spinel group minerals in
562 LL3.00–6 chondrites: Indicators of nebular and parent body processes. *Geochim. Cosmochim.*
563 *Acta* **70**, 5634–5650.

564 Kita N. T. and Ushikubo T. (2012) Evolution of protoplanetary disk inferred from ^{26}Al
565 chronology of individual chondrules. *Meteorit. Planet. Sci.* **47**, 1108–1119.

566 Kita N. T., Nagahara H., Togashi S. and Morishita Y. (2000) A short duration of chondrule
567 formation in the solar nebula: evidence from ^{26}Al in Semarkona ferromagnesian chondrules.
568 *Geochim. Cosmochim. Acta* **64**, 3913–3922.

569 Kita N. T., Nagahara H., Tachibana S., Tomomura S., Spicuzza M. J., Fournelle J. H. and Valley
570 J. W. (2010) High precision SIMS oxygen three isotope study of chondrules in LL3
571 chondrites. *Geochim. Cosmochim. Acta* **74**, 6610–6635.

572 Kita N. T., Ushikubo T., Knight K. B., Mendybaev R. A., Davis A. M., Richter F. M. and
573 Fournelle J. H. (2012) Internal ^{26}Al–^{26}Mg isotope systematics of a Type B CAI. *Geochim.*
574 *Cosmochim. Acta* **86**, 37–51.

575 Kita N. T., Ushikubo T., Tenner T. J., Romaniello S. J. and Wadhwa M. (2016) Instrumental
576 biases for SIMS magnesium isotope analyses. *Goldschmidt conf.*, #1538(abstr.).

577 Kunihiro T., Rubin A. E., McKeegan K. D. and Wasson J. T. (2004) Initial ^{26}Al/^{27}Al in
578 carbonaceous-chondrite chondrules: too little ^{26}Al to melt asteroids. *Geochim. Cosmochim.*
579 *Acta* **68**, 2947–2957.

580 Kurahashi E., Kita N. T., Nagahara H. and Morishita Y. (2008) ^{26}Al–^{26}Mg systematics of
581 chondrules in a primitive CO chondrite. *Geochim. Cosmochim. Acta* **72**, 3865–3882.

582 Ludwig K. R. (2008) User's Manual for Isoplot 3.70. *Berkeley Geochronology Center, Special*
583 *Publication* **4**, 1–76.

584 Mostefaoui S., Kita N. T., Togashi S., Tachibana S., Nagahara H. and Morishita Y. (2002) The
585 relative formation ages of ferromagnesian chondrules inferred from their initial aluminum-
586 26/aluminum-27 ratios. *Meteorit. Planet. Sci.* **37**, 421–438.

587 Nagashima K., Krot A. N. and Huss G. R. (2014) ^{26}Al in chondrules from CR2 chondrites.
588 *Geochem. J.* **48**, 561–570.

589 Nagashima K., Krot A. N. and Komatsu M. (2016) ^{26}Al–^{26}Mg systematics in chondrules from
590 Kaba and Yamato 980145 CV3 carbonaceous chondrites. *Geochim. Cosmochim. Acta*.

591 Nakashima D., Ushikubo T., Joswiak D. J., Brownlee D. E., Matrajt G., Weisberg M. K.,
592 Zolensky M. E. and Kita N. T. (2012) Oxygen isotopes in crystalline silicates of comet Wild
593 2: A comparison of oxygen isotope systematics between Wild 2 particles and chondritic
594 materials. *Earth Planet. Sci. Lett.* **357-358**, 355–365.

595 Nakashima D., Ushikubo T., Kita N. T., Weisberg M. K., Zolensky M. E. and Ebel D. S. (2015)
596 Late formation of a comet Wild 2 crystalline silicate particle, Pyxie, inferred from Al–Mg
597 chronology of plagioclase. *Earth Planet. Sci. Lett.* **410**, 54–61.

598 Newton J., Bischoff A., Arden J. W., Franchi I. A., Geiger T., Greshake A. and Pillinger C. T.
599 (1995) Acfer 094, a uniquely primitive carbonaceous chondrite from the Sahara. *Meteoritics*
600 **30**, 47–56.

601 Norris T. L., Gancarz A. J., Rokop D. J., Thomas, K. W. (1983) Half-Life of ^{26}Al. *J. Geophys.*
602 *Res*. **88**, B331–B333.

603 Pape J., Mezger K., Bouvier A.-S., Baumgartner L. P. (2019) Time and duration of chondrule
604 formation: Constraints from ^{26}Al-^{26}Mg ages of individual chondrules. *Geochim. Cosmochim.*
605 *Acta* **244**, 416–436.

606 Rudraswami N. G., Goswami J. N., Chattopadhyay B., Sengupta S. K. and Thapliyal A. P.
607 (2008) ^{26}Al records in chondrules from unequilibrated ordinary chondrites: II. Duration of
608 chondrule formation and parent body thermal metamorphism. *Earth Planet. Sci. Lett.* **274**,
609 93–102.

610 Russell S. S., Srinivasan G., Huss G. R., Wasserburg G. J. and MacPherson G. J. (1996)
611 Evidence for Widespread ^{26}Al in the Solar Nebula and Constraints for Nebula Time Scales.
612 *Science* **273**, 757–762.

613 Schrader D. L., Nagashima K., Krot A. N., Ogliore R. C., Yin Q.-Z., Amelin Y., Stirling C. H.
614 and Kaltenbach A. (2017) Distribution of ^{26}Al in the CR chondrite chondrule-forming region
615 of the protoplanetary disk. *Geochim. Cosmochim. Acta* **201**, 275–302.

616 Scott E. R. D. and Krot A. N. (2007) 1.07 - Chondrites and their components. In *Treatise on*
617 *Geochemistry, Volume 1: Meteorites, Comets, and Planets* (eds. H. F. Holland and K. K.
618 Turekian). Elsevier, Amsterdam, San Francisco, CA. pp. 1–72.

619 Srinivasan G., Huss G. R. and Wasserburg G. J. (2000) A petrographic, chemical, and isotopic
620 study of calcium-aluminum-rich inclusions and aluminum-rich chondrules from the Axtell
621 (CV3) chondrite. *Meteorit. Planet. Sci.* **35**, 1333–1354.

622 Sugiura N. and Krot A. N. (2007) ^{26}Al-^{26}Mg systematics of Ca-Al-rich inclusions, amoeboid
623 olivine aggregates, and chondrules from the ungrouped carbonaceous chondrite Acfer 094.
624 *Meteorit. Planet. Sci.* **42**, 1183–1195.

625 Tenner T. J., Ushikubo T., Kurahashi E., Kita N. T. and Nagahara H. (2013) Oxygen isotope
626 systematics of chondrule phenocrysts from the CO3.0 chondrite Yamato 81020. *Geochim.*
627 *Cosmochim. Acta* **102**, 226–245.

628 Tenner T. J., Nakashima D., Ushikubo T., Weisberg M. K. and Kita N. T. (2015a) SIMS Al-Mg
629 chronology of CR chondrite chondrules: links with Mg# and O isotopes. *78th Annual Meeting*
630 *of the Meteoritical Society*, #5325(abstr.).

631 Tenner T. J., Nakashima D., Ushikubo T., Kita N. T. and Weisberg M. K. (2015b) Oxygen
632 isotope ratios of FeO-poor chondrules in CR3 chondrites. *Geochim. Cosmochim. Acta* **148**,
633 228–250.

634 Tenner T. J., Kimura M. and Kita N. T. (2017) Oxygen isotope characteristics of chondrules
635 from the Yamato-82094 ungrouped carbonaceous chondrite: Further evidence for common O-
636 isotope environments sampled among carbonaceous chondrites. *Meteorit. Planet. Sci.* **52**,
637 268-294.

638 Ushikubo T., Kimura M., Kita N. T. and Valley J. W. (2012) Primordial oxygen isotope
639 reservoirs of the solar nebula recorded in chondrules in Acfer 094 carbonaceous chondrite.
640 *Geochim. Cosmochim. Acta* **90**, 242–264.

641 Ushikubo T., Nakashima D., Kimura M., Tenner T. J. and Kita N. T. (2013) Contemporaneous
642 formation of chondrules in distinct oxygen isotope reservoirs. *Geochim. Cosmochim. Acta*
643 **109**, 280–295.

644 Ushikubo T., Tenner T. J., Hiyagon H. and Kita N. T. (2017) A long duration of the ^{16}O-rich
645 reservoir in the solar nebula, as recorded in fine-grained refractory inclusions from the least
646 metamorphosed carbonaceous chondrites. *Geochim. Cosmochim. Acta* **201**, 103–122.

van Orman J. A., Cherniak D. J. and Kita N. T. (2014) Magnesium diffusion in plagioclase: Dependence on composition, and implications for thermal resetting of the ^{26}Al–^{26}Mg early solar system chronometer. *Earth Planet. Sci. Lett.* **385**, 79–88.

Villeneuve J., Chaussidon M. and Libourel G. (2009) Homogeneous distribution of ^{26}Al in the Solar System from the Mg isotopic composition of chondrules. *Science* **325**, 985–988.

Weisberg M. K., McCoy T. J. and Krot A. N. (2006) Systematics and Evaluation of Meteorite Classification. In *Meteorites and the Early Solar System II* (eds. D. S. Lauretta and H. McSween). University of Arizona Press, Tucson. pp. 19–52.

Yurimoto H. and Wasson J. T. (2002) Extremely rapid cooling of a carbonaceous-chondrite chondrule containing very ^{16}O-rich olivine and a ^{26}Mg-excess. *Geochim. Cosmochim. Acta* **66**, 4355–4363.

Figure caption

Figure 1: (a) Secondary electron image of marks made by platinum (Pt) deposition and focused ion beam (FIB) milling for helping direct the primary ion beam. (b) Backscattered electron image of SIMS pits in plagioclase of chondrule G63. The Pt deposition marks in (a) are 3×3 μm^2; the FIB marks 1×1 μm^2. Scale bar is 10 μm.

Figure 2: Backscattered electron images of type II chondrules analyzes for their ^{26}Al-^{26}Mg systematics. (a) Large olivine phenocrysts in G9 (IIA) shows oscillatory zoning. (b) G10 (IIA) contains few mesostasis and possesses small, forsteritic olivine relict grains. (c) Slightly zoned olivine phenocrysts and large plagioclase in mesostasis of G61 (IIA). (d) G63 mainly comprises glassy mesostasis and only limited amount of plagioclase. (e) G85 (IIB) shows high-Ca pyroxene overgrowths on low-Ca pyroxene. (f) Large olivine phenocrysts and plagioclase in G86. (g) Small chondrule (G108) with abundant plagioclase. The images show sample surface before oxygen and magnesium isotope analysis of this study. Pre-existing SIMS pits are results of previous studies (Ushikubo et al., 2012; Ushikubo et al., 2013). Scale bar is 100 μm in all images.

Figure 3: BSE images of mesostasis textures. Plagioclase in G9 (a,b) is small and surrounded by high-Ca pyroxene making it difficult to aim the primary ion beam; plagioclase in G10 (c) and G61 (d) is slightly larger. (e) Small plagioclase areas surrounded by olivine; compare with SIMS pits in Fig. 1b. (f,g) Plagioclase in G85 shows minute clinopyroxene microcrystallites. (h,i) Plagioclase in mesostasis of G86 and G108. BSE images show thin section surface before SIMS analysis of this study; pre-existing SIMS pits are from Ushikubo et al. (2012). Scale bar is 10 μm in all images.

Figure 4: Oxygen isotope ratios of individual olivine analyses and the mean values for chondrules in Acfer 094. (a) Graph showing mean chondrule $\Delta^{17}O$ values (stars) and $\Delta^{17}O$ values of individual olivine analyses determined in this study. Some chondrules contain ^{16}O-rich relict olivines. Except for G99, a mean chondrule $\Delta^{17}O$ value was calculated based on three or more isotopically indistinguishable analyses. The homogeneity criterion is illustrated by an error envelope in +/– 0.6‰ distance from chondrule means. Error bars of individual analyses are the external reproducibilities (2SD) of the respective San Carlos olivine standard brackets. (b) Oxygen three-isotope diagram showing the mean values of chondrules from Acfer 094 including data from this study and [1] Ushikubo et al. (2012). The calculation scheme for uncertainties (2SE) is provided in Appendix EA 2. G39 and G85 plot above PCM (Ushikubo et al., 2012) and on TF line. CCAM line: Clayton et al. (1977).

Figure 5: Graph of mean chondrule $\Delta^{17}O$ values and Mg#s in Acfer 094 showing the bimodality of the $\Delta^{17}O$ values. There are two main modes at approximately –5‰ and –2‰ (Ushikubo et al., 2012). Type II chondrules belong either to the –2‰ or 0‰ group; type I chondrules with Mg#s > 97 are mainly members of the –5‰ group. Chondrule G85 and chondrule fragment G39 have $\Delta^{17}O$ values of ~0‰. Uncertainties in Mg#s are the observed range of values (only those points with oxygen isotope data); calculation of uncertainties in $\Delta^{17}O$ values (2SE) is detailed in Appendix EA 2. [1] Data from Ushikubo et al. (2012).

Figure 6: Isochron diagrams and initial $^{26}Al/^{27}Al$ ratios, $(^{26}Al/^{27}Al)_0$, of chondrules. Each chondrule contains plagioclase with resolvable $\delta^{26}Mg^*$. All cited uncertainties in $(^{26}Al/^{27}Al)_0$ include additional 6% or 10% (only G9, G85) uncertainty in RSF because of the different composition of

704 the standards and the unknowns. The error envelopes show 95% confidence limits from the
705 isochron regressions and do not reflect the additional RSF source of uncertainty. Uncertainty in
706 cited initial $^{26}Al/^{27}Al$ ratios are 95%-confidence intervals. Robust regression algorithm was used
707 for isochron of chondrule G108.
708
709 Figure 7: Comparison of initial $^{26}Al/^{27}Al$ ratios of type I and type II chondrules from Acfer 094
710 and Y-81020. (a) Type I and II chondrules from Acfer 094 show the same range of $(^{26}Al/^{27}Al)_0$.
711 The initial $^{26}Al/^{27}Al$ ratio of chondrule G85 is clearly resolvable from that of other type II
712 chondrules. Uncertainties in $(^{26}Al/^{27}Al)_0$ are 95%-confidence intervals. (b) Type II chondrules in
713 Y-81020 tend to be younger than type I chondrules; in contrast, type II chondrules in Acfer 094
714 are not systematically younger. Literature data are from [1] Ushikubo et al. (2013), [2] Kurahashi
715 et al. (2008), and [3] Kunihiro et al. (2004).
716
717 Figure 8: Graphs demonstrating closure of the Al-Mg system in plagioclase. (a) ^{27}Al counts per
718 second per analytical cycle (analysis G9: 3 Plag) closely trace counts of plagioclase standard
719 analyses. Grey area is range of counts per second per each individual cycle observed over all
720 bracketing standards. (b) $^{27}Al/^{24}Mg$ ratio monotonically increases until cycle 36, drops and
721 stabilizes at a new level after cycle 40. Only first 36 cycles are used in data reduction (see Table
722 3). (c) Raw $\delta^{25}Mg_m$ shows undisturbed, monotonically decrease of a typical plagioclase analysis
723 whereas $\delta^{26}Mg_m$ follows abrupt changes of $^{27}Al/^{24}Mg$ ratio. (d) Isochron diagram for chondrule
724 G9. The red diamond represents analysis G9: 3 Plag using cycles 1-36 (open) or 41- 60 (filled
725 symbol) for data reduction. The filled diamond plots on the isochron indicating closed Al-Mg
726 system in both plagioclase domains that were sampled by analysis G9: 3 Plag.

727

728 Figure 9: Mean chondrule $\Delta_{17}O$ values and $(^{26}Al/^{27}Al)_0$ of chondrules form Acfer 094, Y-81020,
729 and ordinary chondrites (LL). The oldest type I and II chondrules from Acfer 094 possess high
730 $\Delta_{17}O$ values that are similar to those of LL chondrites. Literature data from [1] Ushikubo et al.
731 (2012), [2] Ushikubo et al. (2013), [3] Kita et al. (2010), [4] Kita et al. (2000), [5] Kurahashi et al.
732 (2008), and [6] Tenner et al. (2013).

733

Tables

Table 1: Overview of the petrology of the chondrules (all porphyritic) analyzed for oxygen three-isotope ratios and Al-Mg systematics.

Chondrule	Type	Al-Mg dating	Mg#[1] Mean	Mg#[1] Min	Mg#[1] Max	An Mean	An Min	An Max	Glass[2]
G9	IIA	+	48.0	28.1	68.4	14.7	8.2	19.5	
G10	*IIA*	+	*67.8*	*53.3*	*95.9*	52.6	50.6	54.4	
G25	IIA		70.3	64.5	79.0		-		+
G36	IIA		52.0	50.3	53.6	54.4	53.0	56.3	
G61	IIA	+	69.9	62.1	72.9	42.9	37.0	47.4	
G63	*IIA*	+	*62.1*	*52.7*	*86.2*	31.8	29.0	37.5	+
G85	*IIB*	+	*87.1*	*83.9*	*89.6*	18.4	13.5	30.1	
G86	IIA	+	60.0	47.2	70.7	53.8	52.1	56.8	
G88	IIA		69.5	64.4	76.0		-		+
G99	IIA		61.4	56.4	67.5	64.8	62.6	67.4	
G108	IIA	+	52.5	45.8	57.3	39.9	36.4	43.2	
G110	IIA		55.1	45.3	60.1	46.0	43.7	48.3	
G120	IIA		69.0	49.0	86.7		-		+

[1]Full range of Mg#s observed in chondrule. [2]Occurrence of glass in mesostasis. Values shown in italics are from Ushikubo et al. (2012).

Table 2: Mean chondrule Mg#s and oxygen isotope ratios of FeO-rich chondrules in Acfer 094.

Chondrule	N	Mg#[1]		$\delta^{18}O$ ‰		$\delta^{17}O$ ‰		$\Delta^{17}O$ ‰		Ref.
				Mean	Unc.[2]	Mean	Unc.[2]	Mean	Unc.[2]	
G9	8	52	(–19/+14)	1.76	±0.56	–1.22	±0.42	–2.14	±0.24	[1]
G10	*3*	*65*	*(–4/+3)*	*–0.03*	*±1.20*	*–2.79*	*±1.05*	*–2.78*	*±0.53*	[2]
G25	7	69	(–5/+10)	–1.48	±0.45	–4.39	±0.32	–3.62	±0.23	[1]
G36	7	52	(–2/+2)	2.16	±0.32	–1.07	±0.27	–2.19	±0.19	[1]
G61	6	69	(–8/+4)	1.27	±0.39	–1.67	±0.29	–2.33	±0.19	[1]
G63	*3*	*66*	*(–9/+5)*	*- Not calculated -*				*–2.54*	*±0.50*	[2]
G85	*5*	*87*	*(–3/+2)*	*2.70*	*±0.39*	*1.46*	*±0.22*	*0.06*	*±0.25*	[2]
G86	*3*	*63*	*(–1/+1)*	*1.63*	*±0.36*	*–1.49*	*±0.73*	*–2.34*	*±0.61*	[2]
G88	7	69	(–5/+7)	1.78	±0.45	–2.01	±0.45	–2.93	±0.28	[1]
G99	5	62	(–5/+6)	- Not calculated -						[1]
G108	3	54	(–1/+1)	2.43	±0.47	–0.93	±0.27	–2.19	±0.22	[1]
G110	4	57	(–3/+3)	2.30	±0.58	–0.87	±0.61	–2.07	±0.34	[1]
G120	6	71	(–14/+16)	1.38	±0.84	–1.69	±0.64	–2.40	±0.29	[1]

[1]Only Mg#s of those olivine grains used to calculate the mean chondrule isotope ratios; values in parenthesis show range. [2]Calculations of uncertainties are reported in EA 2. Data from [1] this study and [2] Ushikubo et al. (2012).

744 Table 3. Results of ^{26}Al-^{26}Mg isotope analysis of type II chondrules in Acfer 094.

Chondrule	Spot#	Phase	^{27}Al/^{24}Mg	Unc.[1]	δ^{26}Mg*	Unc.[1]	Cycles[2]
G9, IIA	1	Plag	931	101	26.8	5.3	17
	2	Plag	527	59	12.6	4.9	13
	3	Plag	965	114	28.6	4.1	36
	4	Plag	1259	151	31.4	5.7	27
	5	Plag	139	15	1.4	3.7	12
	6	Ol	0.0011	0.0001	0.03	0.08	
	7	Ol	0.0010	0.0001	–0.09	0.08	
	8	Ol	0.0011	0.0001	–0.11	0.08	
	53	Ol	0.0011	0.0001	0.00	0.08	
G10, IIA	9	Plag	221	14	9.0	1.8	60
	10	Plag	214	13	7.1	2.2	40
	11	Plag	211	15	6.4	2.2	60
	12	Plag	250	19	8.0	5.1	11
	13	Ol	0.0015	0.0001	0.02	0.08	
	14	Ol	0.0036	0.0004	0.05	0.08	
	15	Ol	0.0014	0.0001	–0.08	0.08	
G61, IIA	16	Plag	207	13	6.9	1.9	60
	17	Plag	173	11	6.1	1.8	60
	18	Plag	201	12	8.8	2.7	60
	19	Plag	146	12	7.1	2.8	17
	20	Ol	0.0015	0.0001	–0.04	0.08	
	21	Ol	0.0016	0.0002	–0.03	0.08	
	22	Ol	0.0017	0.0002	0.03	0.08	
	54	Ol	0.0016	0.0002	–0.01	0.08	
G63, IIA	23	Plag	212	26	7.5	2.6	16
	24	Plag	300	34	10.3	2.3	60
	25	Plag	282	21	8.8	2.9	39
	26	Ol	0.0017	0.0002	–0.04	0.06	
	27	Ol	0.0017	0.0002	–0.03	0.06	
	28	Ol	0.0018	0.0002	–0.02	0.06	
	55	Ol	0.0026	0.0003	0.00	0.08	
G85, IIB	29	Plag	1696	195	112.0	4.5	60
	30	Plag	600	70	43.3	5.9	21
	31	Plag	687	90	45.6	3.9	34
	32	Plag	710	86	49.7	13.0	5
	33	Plag	103	18	5.8	2.9	20
	34	Lpx	0.0235	0.0024	0.00	0.08	
	35	Lpx	0.0047	0.0005	–0.02	0.08	
	36	Lpx	0.0130	0.0013	–0.08	0.08	

G86, IIA	37	Plag	202	13	4.9	3.1	25
	38	Plag	196	12	5.1	2.2	60
	39	Plag	167	12	3.8	2.3	60
	40	Plag	227	15	6.3	2.3	60
	41	Ol	0.0014	0.0001	–0.05	0.05	
	42	Ol	0.0031	0.0003	–0.01	0.07	
	43	Ol	0.0017	0.0002	–0.01	0.06	
	56	Ol	0.0020	0.0002	–0.01	0.08	
G108, IIA	44	Plag	219	15	4.6	2.2	60
	45	Plag	227	14	5.7	2.2	60
	46	Plag	129	8	2.3	2.2	60
	47	Plag	226	15	6.2	2.3	60
	48	Plag	264	19	6.3	2.5	41
	49	Plag	231	17	7.8	2.2	60
	50	Ol	0.0012	0.0001	0.01	0.08	
	51	Ol	0.0013	0.0001	–0.01	0.07	
	52	Ol	0.0006	0.0001	–0.14	0.06	

[1]Uncertainties quoted are at the 2σ level including uncertainties of RSF and instrumental bias corrections.
[2]Number of cycles for plagioclase analyses that are included in data reduction.

748 Table 4: Results of isochron regressions for type II chondrules in Acfer 094[1].

Chondrule	$(^{26}Al/^{27}Al)_0$[2]	$(\delta^{26}Mg)^*_0$ [‰]	MSWD	Age rel. to CAI [Ma][3]
G9, IIA	$(3.80 \pm 0.54) \times 10^{-6}$	-0.04 ± 0.04	1.9	2.66 (–0.13/+0.15)
G10, IIA	$(4.96 \pm 0.78) \times 10^{-6}$	0.00 ± 0.05	1.7	2.39 (–0.15/+0.17)
G61, IIA	$(5.22 \pm 0.87) \times 10^{-6}$	-0.01 ± 0.04	0.74	2.34 (–0.16/+0.18)
G63, IIA	$(4.70 \pm 0.82) \times 10^{-6}$	-0.03 ± 0.03	0.25	2.45 (–0.16/+0.19)
G85, IIB	$(9.3 \pm 1.1) \times 10^{-6}$	-0.03 ± 0.04	0.68	1.75 (–0.11/+0.12)
G86, IIA	$(3.62 \pm 0.86) \times 10^{-6}$	-0.03 ± 0.03	0.42	2.71 (–0.22/+0.28)
G108, IIA[4]	$(3.7\ ^{+1.1}_{-0.8}) \times 10^{-6}$	$-0.14\ ^{+0.15}_{-1.4}$	-	2.69 (–0.27/+0.25)

749 [1]Quoted uncertainties are 95%-confidence intervals. [2]6% or 10% (only G9, G85) uncertainties in
750 RSFs are included. [3]Relative ages after the formation of CAIs by assuming a canonical $(^{26}Al/^{27}Al)_0$
751 of 5.2×10^{-5} (Jacobsen et al., 2008) of CAIs. [4]Robust regression algorithm of Isoplot macro
752 (Ludwig, 2008) used.

753

754 Table 5: Compilation of mean Mg#s, oxygen isotope ratios, and initial $^{26}Al/^{27}Al$ ratios of type I
755 and II chondrules from in Acfer 094.

Ch	Mg#	$\delta^{18}O$ ‰		$\delta^{17}O$ ‰		$\Delta^{17}O$ ‰		$(^{26}Al/^{27}Al)_0$ [1]	Ref.
		Mean	Unc.[2]	Mean	Unc.[2]	Mean	Unc.[2]	$\times 10^{-6}$	
Type II chondrules									
G9	52	1.76	±0.56	–1.22	±0.42	–2.14	±0.24	(3.80 ± 0.54)	[1]
G10	*65*	*–0.03*	*±1.20*	*–2.79*	*±1.05*	*–2.78*	*±0.53*	(4.96 ± 0.78)	[1, 2]
G61	69	1.27	±0.39	–1.67	±0.29	–2.33	±0.19	(5.22 ± 0.87)	[1]
G63	*66*	*- Not calculated -*				*–2.54*	*±0.50*	(4.70 ± 0.82)	[1, 2]
G85	*87*	*2.70*	*±0.39*	*1.46*	*±0.22*	*0.06*	*±0.25*	(9.3 ± 1.1)	[1, 2]
G86	*63*	*1.63*	*±0.36*	*–1.49*	*±0.73*	*–2.34*	*±0.61*	(3.62 ± 0.86)	[1, 2]
G108	54	2.43	±0.47	–0.93	±0.27	–2.19	±0.22	(3.7 +1.1/–0.8)	[1]
Type I chondrules									
G15*	99	–3.74	±0.85	–6.59	±0.44	–4.64	±0.42	(6.0 ± 1.7)	[2, 3]
G18	98	–6.51	±0.92	–8.71	±0.67	–5.33	±0.65	(4.7 ± 2.8)	[2, 3]
G39	92	3.12	±0.51	1.12	±0.39	–0.51	±0.37	(9.0 ± 1.5)	[2, 3]
G45	95	0.66	±0.39	–2.08	±0.38	–2.42	±0.36	(4.2 ± 2.0)	[2, 3]
G46	99	–4.59	±0.53	–7.27	±0.39	–4.88	±0.29	(4.7 ± 2.7)	[2, 3]
G68	98			- Not calculated -				(5.0 ± 2.2)	[2, 3]
G73	99	–6.80	±0.81	–9.70	±0.54	–6.16	±0.24	(7.6 ± 1.8)	[2, 3]
G74	95	1.50	±0.61	–1.15	±0.44	–1.93	±0.25	(5.6 ± 2.0)	[2, 3]
G76	99	–3.47	±0.40	–6.88	±0.84	–5.08	±0.78	(5.1 ± 2.7)	[2, 3]
G95	99	–3.41	±0.37	–6.54	±0.26	–4.77	±0.26	(4.9 ± 1.5)	[2, 3]

756 [1]Uncertainties are 95%-confidence intervals. [2]Calculation of uncertainties are reported in EA 2.
757 *Al-rich chondrule. Data from [1] this study, [2] Ushikubo et al. (2012), and [3] Ushikubo et al.
758 (2013)
759

EA captions

Appendix EA 1: EPMA analyses of plagioclase

Appendix EA 2: Additional analytical detail

Appendix EA 3: SIMS oxygen isotope analyses of olivine

Appendix EA 4: Oxygen three-isotope diagrams for individual chondrules

Appendix EA 5: Position of SIMS measurements (Oxygen three isotopes)

Appendix EA 6: SIMS magnesium isotope data set, isochron calculation

Appendix EA 7: Position of SIMS measurements (Al-Mg chronometry)

Appendix EA 8: Additional figures

Appendix EA 9: BSE mosaic of the Acfer 094 USNM 7233-6 thin section that shows locations of chondrules discussed in the article.

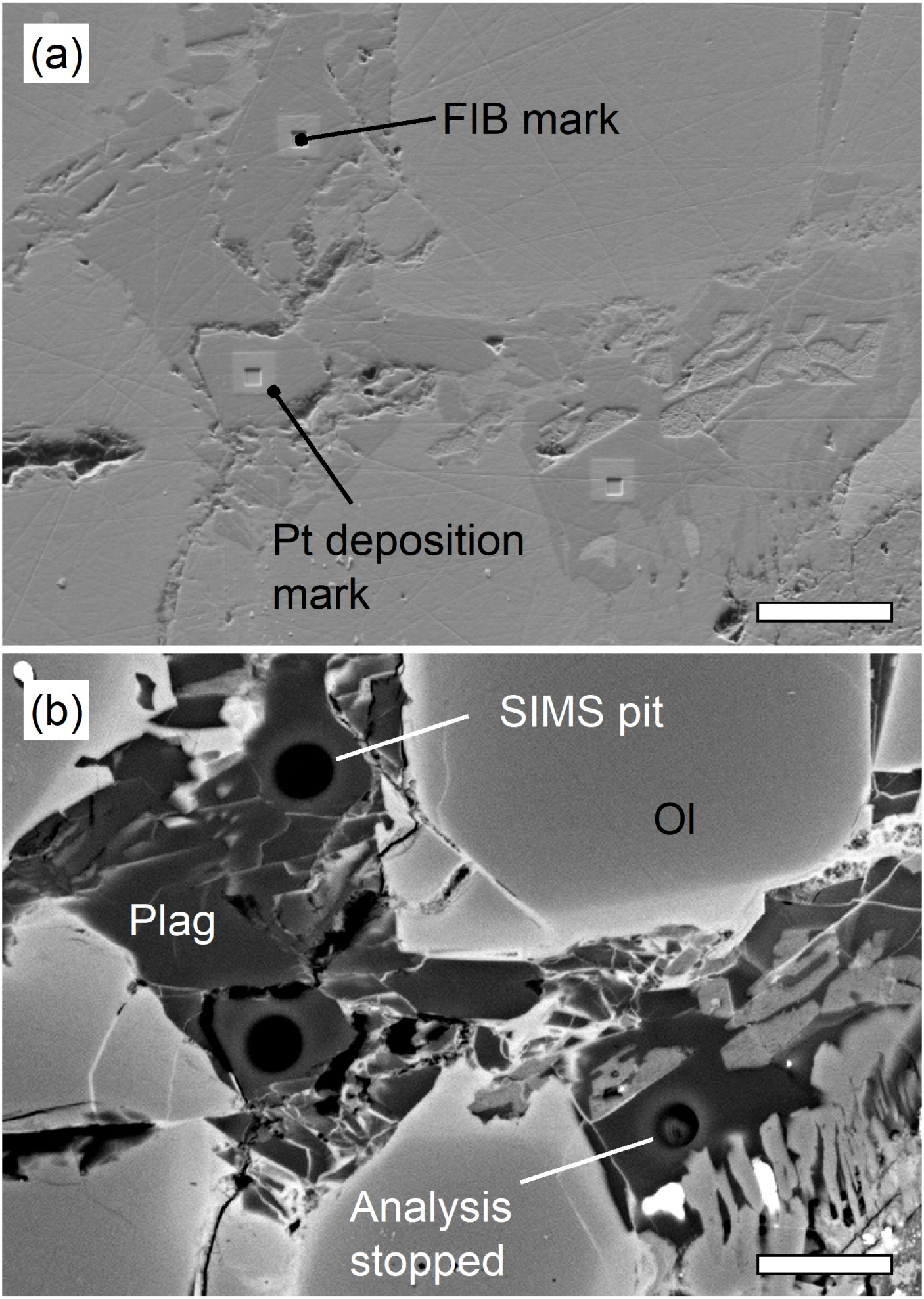
(a)
FIB mark
Pt deposition mark
(b)
SIMS pit
Ol
Plag
Analysis stopped

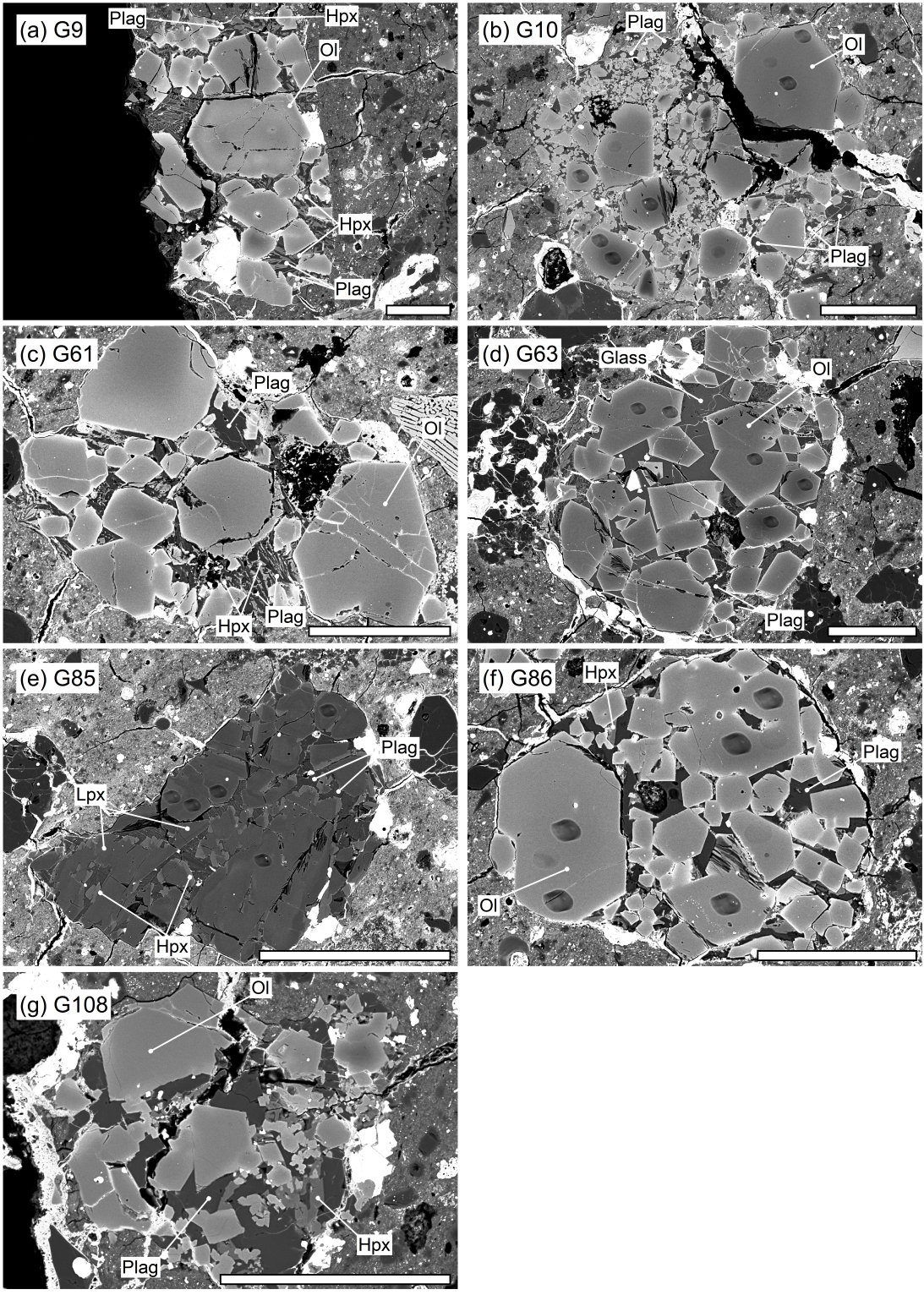
(a) G9
Plag
Hpx
Ol
Hpx
Plag
(b) G10
Plag
Ol
Plag
(c) G61
Plag
Ol
Hpx
Plag
(d) G63
Glass
Ol
Plag
(e) G85
Plag
Lpx
Hpx
(f) G86
Hpx
Plag
Ol
(g) G108
Ol
Hpx
Plag

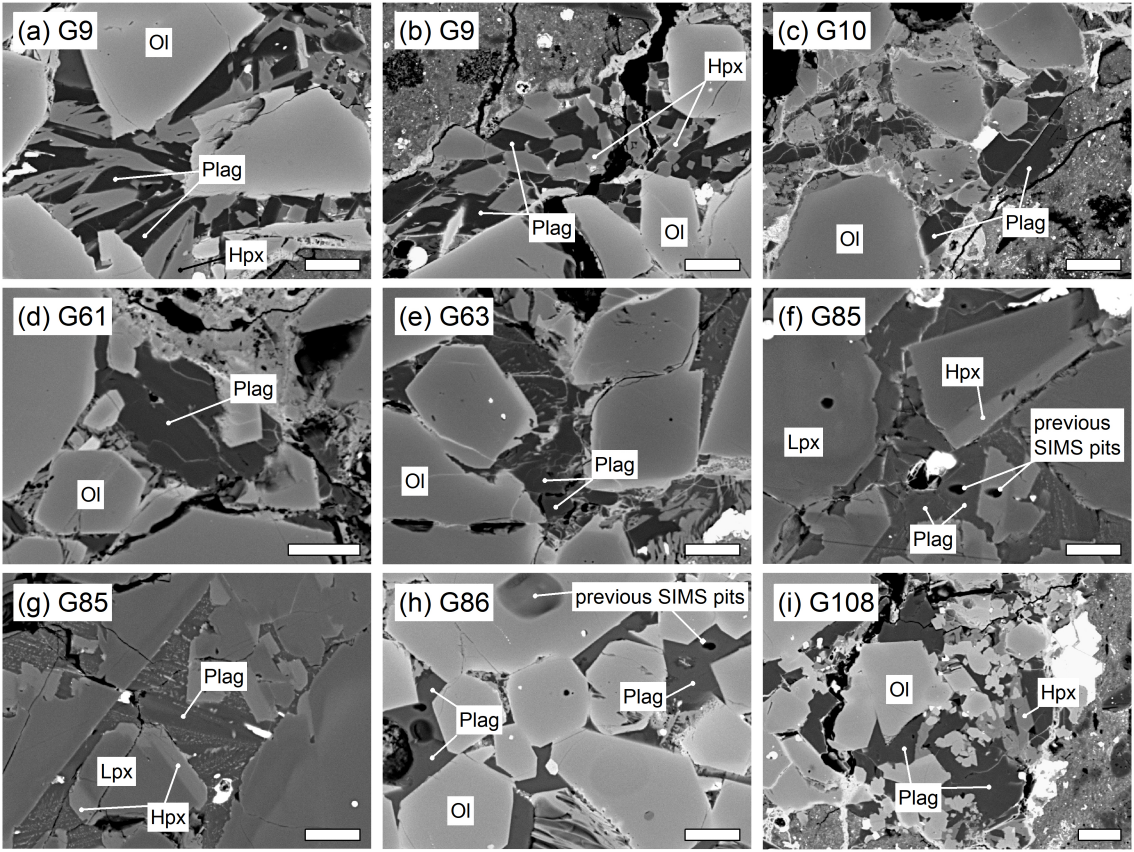
(a) G9
Ol
Plag
Hpx
(b) G9
Hpx
Plag
Ol
(c) G10
Ol
Plag
(d) G61
Plag
Ol
(e) G63
Ol
Plag
(f) G85
Hpx
Lpx
previous SIMS pits
Plag
(g) G85
Plag
Lpx
Hpx
(h) G86
previous SIMS pits
Plag
Plag
Ol
(i) G108
Ol
Hpx
Plag

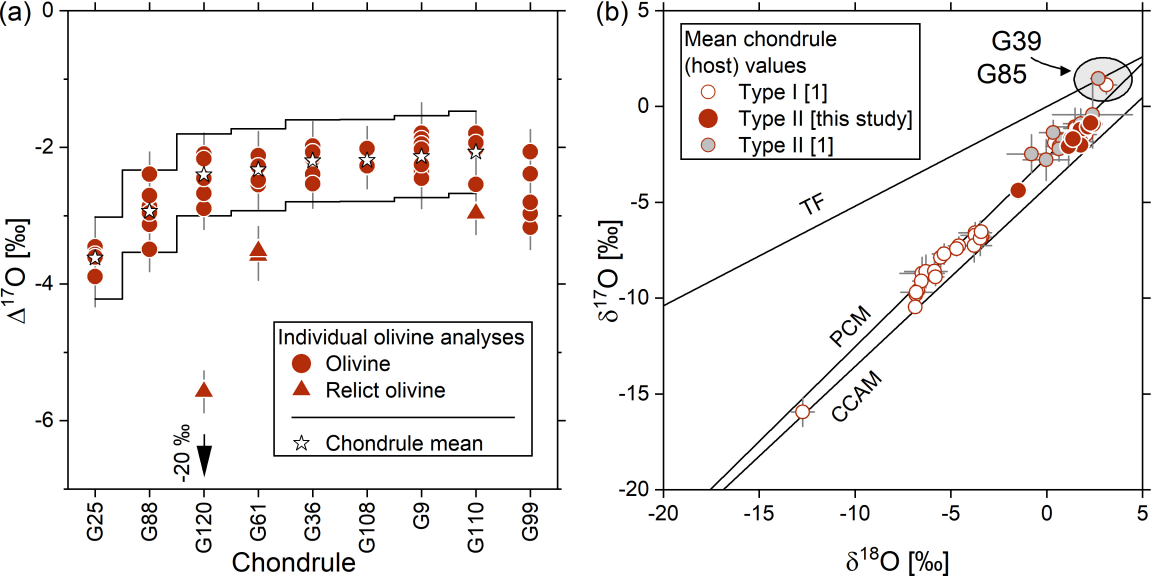
(a)
0
-2
-4
-6
Δ17O [‰]
Individual olivine analyses
Olivine
Relict olivine
Chondrule mean
-20 ‰
G25
G88
G120
G61
G36
G108
G9
G110
G99
Chondrule
(b)
Mean chondrule (host) values
Type I [1]
Type II [this study]
Type II [1]
G39
G85
TF
PCM
CCAM
δ17O [‰]
δ18O [‰]
5
0
-5
-10
-15
-20

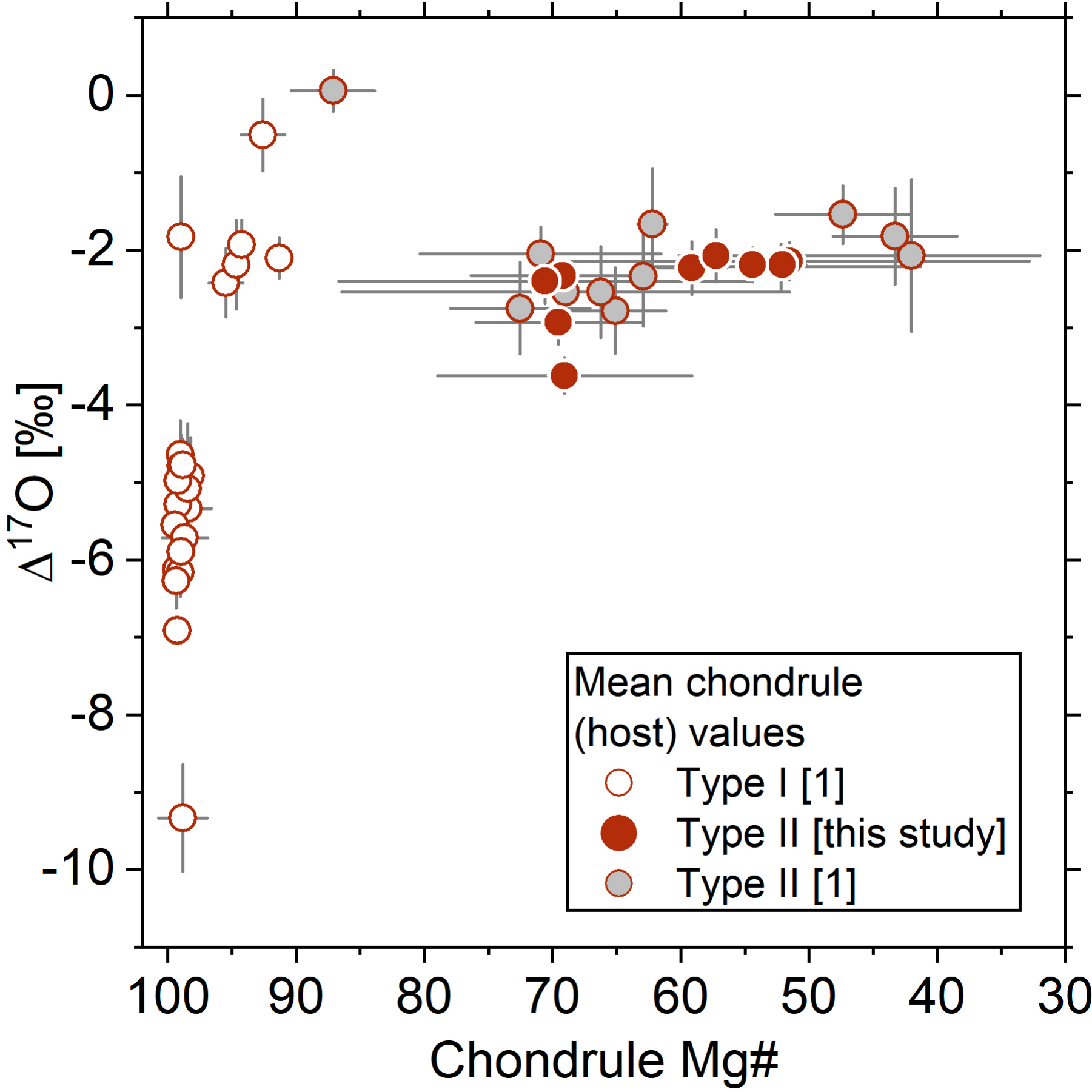
0
-2
-4
-6
-8
-10
Δ17O [‰]
100
90
80
70
60
50
40
30
Chondrule Mg#
Mean chondrule
(host) values
Type I [1]
Type II [this study]
Type II [1]

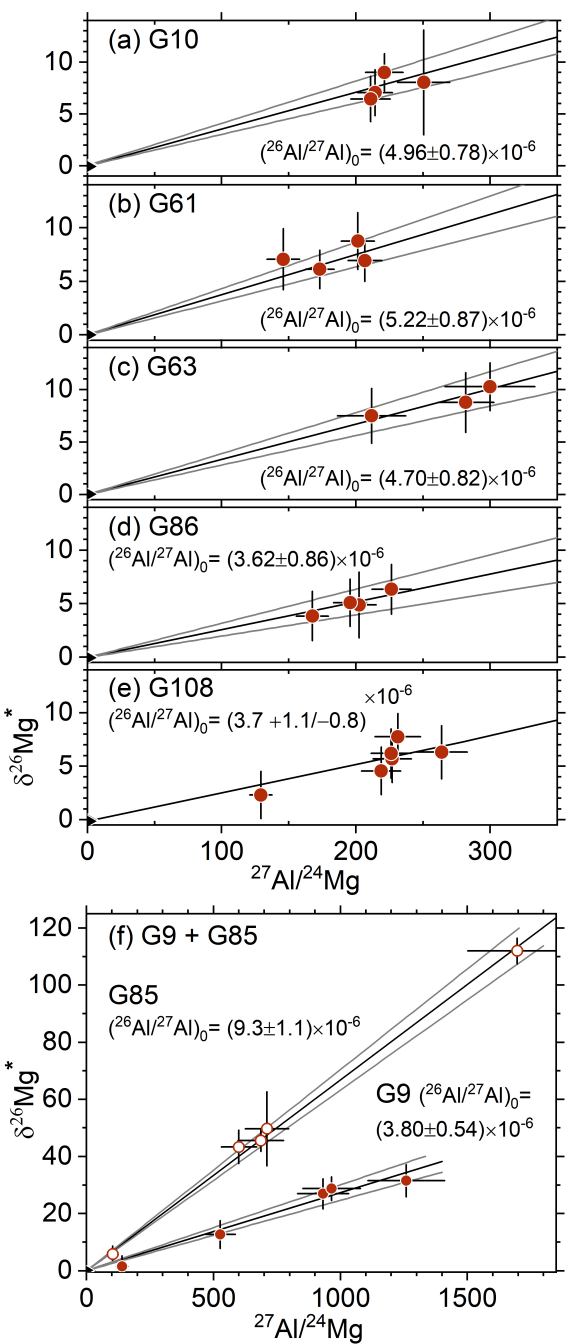
(a) G10
$(^{26}Al/^{27}Al)_0$= (4.96±0.78)×10^{-6}
(b) G61
$(^{26}Al/^{27}Al)_0$= (5.22±0.87)×10^{-6}
(c) G63
$(^{26}Al/^{27}Al)_0$= (4.70±0.82)×10^{-6}
(d) G86
$(^{26}Al/^{27}Al)_0$= (3.62±0.86)×10^{-6}
(e) G108
×10^{-6}
$(^{26}Al/^{27}Al)_0$= (3.7 +1.1/−0.8)
δ^{26}Mg*
^{27}Al/^{24}Mg
(f) G9 + G85
G85
$(^{26}Al/^{27}Al)_0$= (9.3±1.1)×10^{-6}
G9 $(^{26}Al/^{27}Al)_0$= (3.80±0.54)×10^{-6}
δ^{26}Mg*
^{27}Al/^{24}Mg

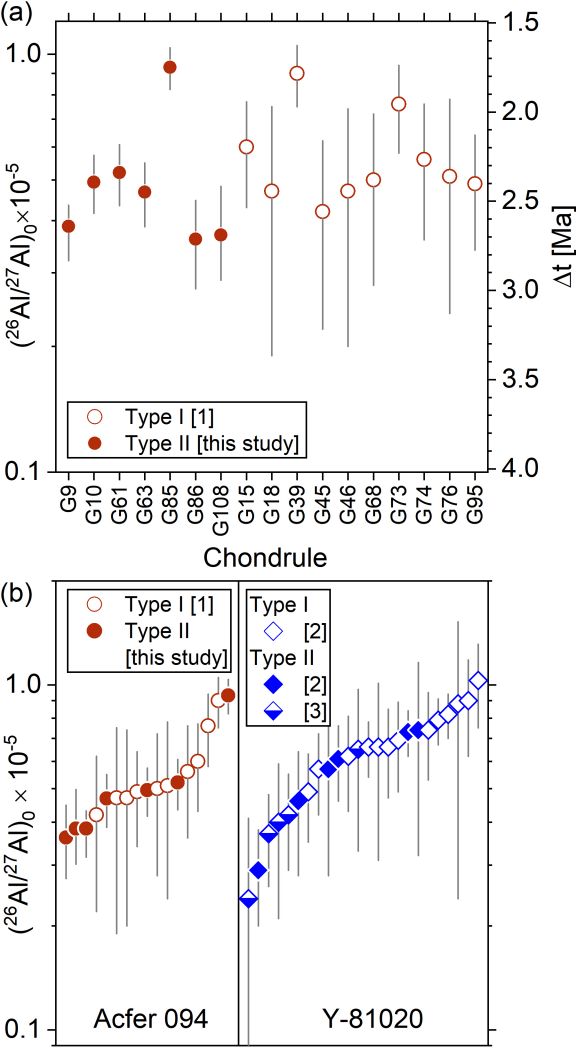
(a)
1.0
0.1
$(^{26}Al/^{27}Al)_0 \times 10^{-5}$
1.5
2.0
2.5
3.0
3.5
4.0
Δt [Ma]
Type I [1]
Type II [this study]
G9
G10
G61
G63
G85
G86
G108
G15
G18
G39
G45
G46
G68
G73
G74
G76
G95
Chondrule
(b)
Type I [1]
Type II
[this study]
Type I
[2]
Type II
[2]
[3]
1.0
0.1
$(^{26}Al/^{27}Al)_0 \times 10^{-5}$
Acfer 094
Y-81020

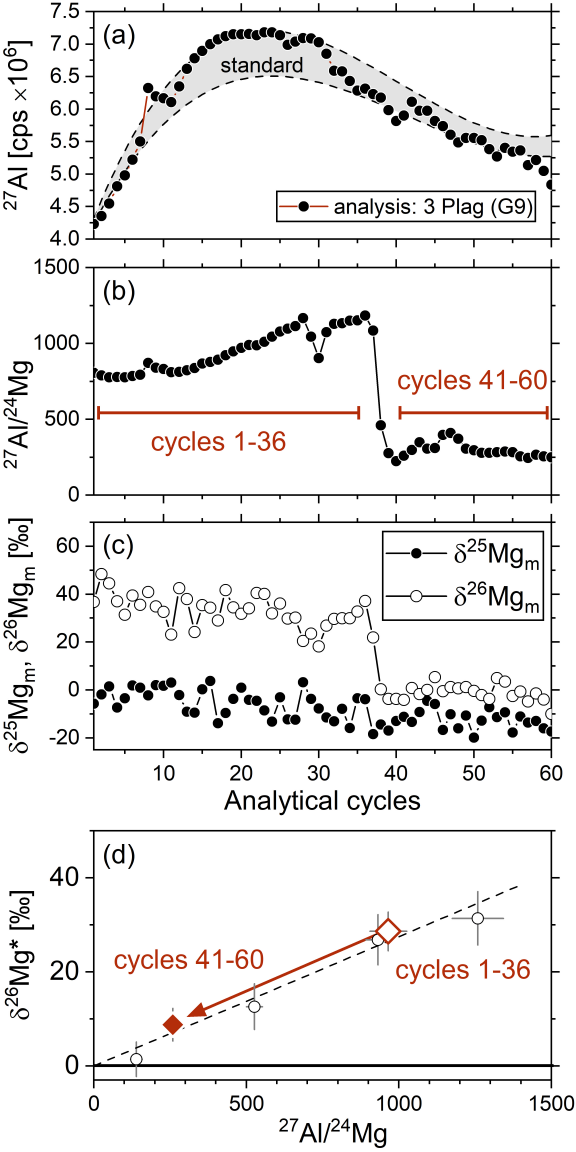
(a)
standard
analysis: 3 Plag (G9)
^{27}Al [cps ×10^6]
(b)
cycles 41-60
cycles 1-36
^{27}Al/^{24}Mg
(c)
$\delta^{25}Mg_m$
$\delta^{26}Mg_m$
$\delta^{25}Mg_m$, $\delta^{26}Mg_m$ [‰]
Analytical cycles
(d)
cycles 41-60
cycles 1-36
$\delta^{26}Mg^*$ [‰]
^{27}Al/^{24}Mg

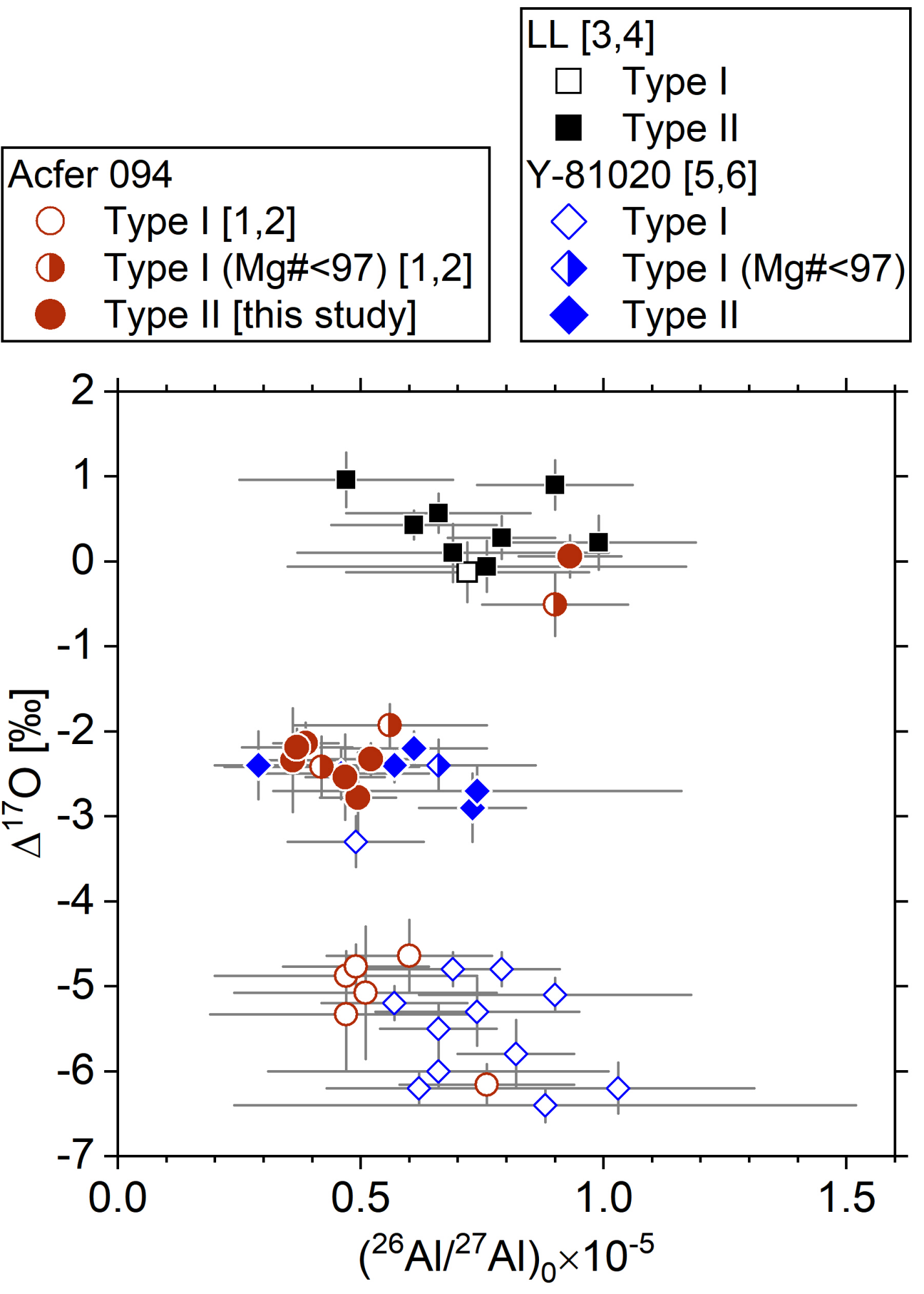
Acfer 094
Type I [1,2]
Type I (Mg#<97) [1,2]
Type II [this study]
LL [3,4]
Type I
Type II
Y-81020 [5,6]
Type I
Type I (Mg#<97)
Type II
2
1
0
-1
-2
-3
-4
-5
-6
-7
Δ17O [‰]
0.0
0.5
1.0
1.5
(26Al/27Al)0×10-5